May 2015

Improving Galvanizing Bath Hardware

Amir Kargar Neghab,

Supervisor: Dr. Andrew Hrymak, *The University of Western Ontario*
A thesis submitted in partial fulfillment of the requirements for the Master of Engineering Science degree in Chemical and Biochemical Engineering

Improving Galvanizing Bath Hardware

(Thesis format: Monograph)

by

Amir Kargar Neghab

Graduate Program in Chemical and Biochemical Engineering

A thesis submitted in partial fulfillment
of the requirements for the degree of
Masters of Engineering Science

The School of Graduate and Postdoctoral Studies
The University of Western Ontario
London, Ontario, Canada

Abstract

Suspended dross particles in galvanizing bath can interact with moving rolls that guide the strip and eventually accumulate on it. They can cause the roll to function improperly and reduce the surface quality of galvanized steel sheet.

In this research, a turbulent flow simulation of a continuous sheet galvanizing bath is carried out using the computational fluid mechanics in Ansys FLUENT to determine the flow profile inside a galvanizing bath. Multiphase flow modeling has been performed to understand the particle-surface interactions by coupling the particulate models for solid phase with computational fluid dynamics for fluid phase.

A strong fluid flow along the roll axis, which captures a significant number of dross particles, was found in the 3D bath simulation. It was observed that surface region in which particles agglomerate on the roll reported by the industry is the same as where particles collisions with the roll were observed in the simulation.

Keywords

CFD simulation, multiphase flow, galvanizing bath, dross particle, groove pattern

Acknowledgments

I would like to extend my gratitude to the many people who helped me to complete this research project.

Foremost, I would like to sincerely thank my advisor, Dr. Andrew Hrymak for his continual supervision and guidance throughout my program and for providing me the opportunity of obtaining a graduate degree at Chemical Engineering Department at Western University.

I am also grateful for valuable assistance and financial support of Dr. Frank Goodwin and International Lead Zinc Organization throughout this research project. I would also like to acknowledge the guidance of Professor Anthony Straatman and the valuable questions he raised. I sincerely thank the examination committee Dr. Mita Ray and Dr. Cedric Briens.

Special thanks to my supportive and caring wife, Mehraneh for giving me the motivation and confidence and also my parents, my sisters and my in-laws for their faith and continuous support. Lastly, I would like to thank my best friends and intellectual partners Ethan Doan and Pooya Mirzabeygi for being there for me personally and academically.

Table of Contents

List of Tables

List of Figures

Nomenclature

Roman Letters

A	particle projected area
C_t	tangential dashpot coefficients
CD	drag coefficient
$C_{\varepsilon 1}, C_{\varepsilon 2}, C_{\mu}, \sigma_{\varepsilon}, \sigma_k$	model constants
d	diameter, m
f	body force per unit mass, N/kg
F_D	drag force N
F_x	acceleration force
g	gravitational acceleration, m/s2
I	particle moment of inertia
k	turbulent kinetic energy, m2/s2
K_t	tangential spring coefficients
m	particle mass
P	pressure, Pa
Re	Reynolds number
t	time, s
u	velocity, m/s
u_*	friction velocity
V_c	critical velocity
X	location parameter
Y	distance from wall
Y^+	wall coordinate

Greek Letters

Δ	change in a property
∇	gradient
ε	dissipation rate, m^2/s^3
μ	dynamic viscosity of a fluid, kg/m.s

ρ	density, kg/m^3
ω	particle rotational velocity
τ	stress, N/m^2
μ	static coefficient
δ	distance, m
σ	surface tension

Subscripts

k	turbulent kinetic energy
ε	dissipation rate
p	particle
f	fluid

Abbreviations

DEAL	Determining Effective Aluminum
DEM	Discrete Element Method
DPM	Discrete Particle Method
MAP	Modeling Aluminum Pick-up
RANS	Reynolds Averaged Navier Stokes
PIV	Particle Image Velocimetry
SWF	Standard Wall Function
VOF	Volume of Fluid

Chapter 1

1.1 Introduction

Zinc has been used as one of the most important materials to improve the corrosion durability and performance of steel. This improvement is provided by the process of coating of steel. Hot-dip coating has been found to be one of the most economical methods for steel protection from the corrosion phenomenon.

Galvanized steel sheets are produced in a complex metallurgical process known as continuous hot-dip galvanizing process. Galvanized steel can be found in almost every industry that uses steel including utilities, paper industry, household appliances, construction materials and any other industry where the final products are subject to outdoor exposure. However, the most important product in the market is the galvanized steel used in automotive industry. Almost 75% of all galvanized steel sheet is produced for auto body and the remaining percentage is used for other purposes [1].

Some of the unique properties of galvanized steel are: corrosion resistance, low initial cost, long life, formability, reliability, recyclability, light weight and high strength.

1.2 Galvanizing Process Description

Continuous hot-dip galvanizing is a complex metallurgical process which involves continuous submersion of steel sheet in a molten zinc bath resulting in coating of the steel sheet. Galvanizing process consists of 4 basic steps: surface preparation, Annealing, galvanizing and inspection. The most critical part in the industrial galvanizing line is where the actual metallurgical reaction between the steel and the zinc takes place. This study focuses on the galvanizing bath. Figure 1-1 displays a schematic continuous hot-dip galvanizing line.

In a typical hot-dip galvanizing line [2], the steel strip is first uncoiled and then welded to the previous sheet coil to keep the production continuous. After the cleaning process in the pre-treatment section, the strip is rinsed and dried to enter to the furnace to increase its strength and formability. The strip is now ready to enter to the hot-dip galvanizing bath.

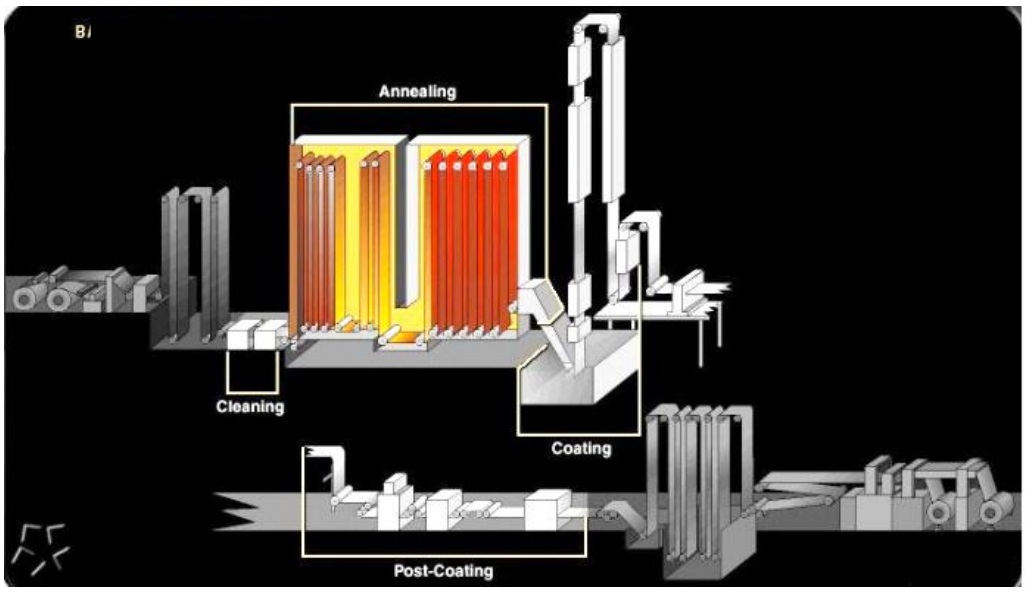

Figure 1- 1: Continuous hot-dip galvanizing line

The most critical part in the industrial galvanizing line is where the actual metallurgical reaction between the steel and the zinc takes place.

As shown Figure 1-2, a galvanizing bath contains a snout, a sink roll, two guide rolls which are supported by bearings. In the galvanizing bath, steel is submerged into the molten zinc at speeds ranging between 1 to 3m/s through snout. The strip speed depends on the design of the galvanizing line and its application. The steel strip reacts with the molten zinc alloy at a temperature between 450°C and 480°C to form a protective coating layer on the steel surface.

Generally, once the strip exits the bath, the excess molten zinc is removed from the strip by the wiping air knives. Air knives produce high pressure jets of air (or nitrogen gas) to control the coating thickness. Then the product goes to the post treatment section.

In the galvanizing bath, intermetallic compounds in the form of dross particles are generated through chemical reactions in the bath. These particles can collide with the bath hardware components and eventually agglomerate. One of the main reasons for roll failure is dross build-up on the surface of the sink roll. The main locations of agglomeration reported by industry are at the bottom of the bath and on the surface of the sink roll.

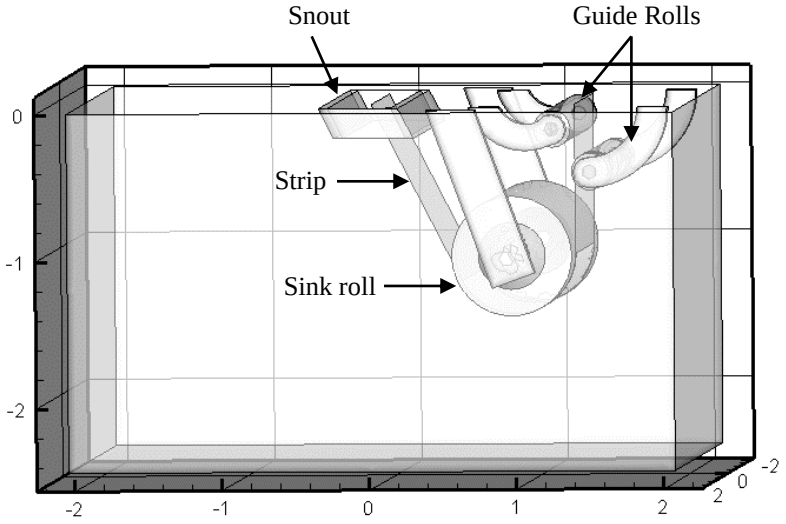

Figure 1- 2: Geometry of galvanizing bath

This degradation can stop the operation of the galvanizing line and reduce the coating quality of the steel sheets. Dross build-up increases the maintenance cost and shut down time for replacement of the defective hardware components. The cost of re-running a galvanizing line due to failure is roughly estimated to be around $1000 per hour [3] in addition to loss of production, energy and profit.

1.3 Dross Particle

Isolated intermetallic particles known as dross are generated in the galvanizing bath through chemical reactions between molten zinc, aluminum, and iron. These particles can reduce the surface quality of galvanized steel sheet [4].

As shown in Figure 1-2, the steel sheet to be galvanized is guided by the guide rolls and sink roll in the bath. The coating quality of the steel sheets is affected by the surface of the moving sink roll in the bath, since these floating dross particles tend to agglomerate on the sink roll. Therefore, the quality and the performance of the sink roll surface correspond to the quality of the steel produced.

The density of the dross particles depends on the Al content in the bath. The dross particle rich in Al, is known as *top dross* and the one rich in Zn and low in Al, is known as *bottom dross*.

Top dross has chemical formulations of $Fe_2Al_5Zn_x$ or $Fe_2Al_{5-x}Zn_x$, size of 10-20 μm and density of 4600 kg/m^3 forms mainly at the top of the bath. Whereas, bottom dross known as $Fe_2Zn_7Al_y$ /$FeZn_{10}Al_y$ with size of 100 μm and a density of 7200 kg/m^3 is generated at the bottom of the bath [5].

Varadaranjan and Kang [3] discuss how dross particles can agglomerate on the roll surface and on the sink roll pinion arm resulting in surface coating imperfections.

1.4 Primary sources of dross formation

Dunbar [7] and Kim *et al.* [8] suggested that possible source of the dross formation is the reactions of the zinc with iron fines on the strip surface. However, further studies prove that the dissolution of iron from the surface of steel strip is the main source of dissolved iron [9] .

Main sources of dross formation in the bath can be categorized as:

- Any small fluctuations in temperature will result in dross generation since local decreases in the bath temperature reduce the solubility of the iron which make the molten zinc supersaturated with iron [10]. Direct continuous contact of steel strip and molten zinc causes the molten zinc to be saturated with iron. Thus, any iron in excess of the zinc's solubility limit is converted into dross particles [4].
- The turbulent flow inside the bath will cause the dross particles to be deposited (due to their inertial forces) on the bath hardware surfaces, mainly on the sink roll surface [11].

1.5 Goal of this project

Studying fluid flow patterns in the hot-dip galvanizing bath has a great importance in understanding the particle-surface interaction. The surface quality and the performance of the moving rolls are relevant to the quality of the produced steel sheet.

The goal of this project is to model dross particle agglomeration in a galvanizing bath through CFD studies. Since we cannot model the complex particle agglomeration on the sink roll, we study particle trajectories and particle-surface interactions. This research is aimed at understanding the dross particle trajectories and also how they collide with the roll surface in a continuous hot-dip galvanizing bath line using CFD techniques. In order to study the particle build-up mechanism, which is very complex, a hypothesis has been made. The hypothesis was based on the assumption that the location of the particles collision with the roll surface is indicative of where dross particles agglomerate on the roll.

Three-dimensional simulations of the bath fluid flow in a galvanizing bath have been undertaken; so as to:

1. Study the bulk flow pattern inside the bath
2. Enable near roll surface studies; i.e. at locations in the immediate proximity as well as at a distance from the strip-roll contact
3. Study different groove geometries on the moving sink roll
4. Study the bath fluid flow at the free surface of the bath

1.6 Outline of thesis

The remaining chapters of the thesis are as follows:

- **Chapter 2**

  The literature review shows the validity of using CFD for the study of 3D bath flow in the galvanizing bath. In this chapter, previous numerical simulations and experimental studies on the galvanizing bath have been presented and summarized.

- **Chapter 3**

  In this chapter, governing equations for fluid flow solution of the galvanizing bath have been explained. Different approaches of multiphase flow modeling including particle equation of motion, are also mentioned.

- **Chapter 4**

  In this chapter, two different levels of fluid flow study have been performed: general fluid flow structure in the bath and detailed flow behaviour in the near vicinity of the roll. To understand how dross particles interact with the hardware components, it is important to elaborate on the tracking of dross particles

- **Chapter 5**

  Based on an extensive literature review on the influence of the groove geometry on particle build-up, it was found that there have been few studies on the effect of the groove. Hence, this section is aimed at better understanding of groove. A CFD simulation has been conducted for some grooves using simplified transverse fluid flow. A simplified block-strip study has been performed in order to determine the fluid flow behaviour at the groove entrance and potential effects on particles.

- **Chapter 6**

  Normally, the bath surface is modeled very simply as a zero normal velocity boundary condition. In this chapter, the free surface (liquid-air) fluid is modeled. This study will allow us to understand the fluid flow at the meniscus at the strip entry and exit region as well as modeling of wave motion at the free surface. Air-entrainment is also discussed with the relevant formulations.

- **Chapter 7**

  Conclusions of the present study along with the contributions made and some recommendations for future work.

Chapter 2

2 Literature Review

This literature survey provides a general review on the use of CFD in fluid flow modeling of the galvanizing bath. Numerical simulations have been conducted for the fluid flow in some continuous galvanizing baths. There are also a number of experimental studies using cold models that examine the flow field inside the bath. Some of these studies are presented in this section.

2.1 Previous Studies

A half-scale water model of an industrial bath was reported by Gagné *et al.* [11] using Plexiglas material with a circulating rubber belt to simulate the steel strip motion. Fluid flow patterns within the bath were observed by tracking the polymeric particle motion using a video camera.

Kurobe *et al*. [12] performed an experimental study by using polystyrene particles as top and bottom dross particles, and NaCl solution as the molten zinc to examine the particle motion in the bath. They showed that dross particles become concentrated in the "V-section" above the sink roll, between the steel strip entry and exit region.

Shin *et al.* [13] made a one-tenth transparent scale cold water model to understand the bath flow structure using PIV techniques. They focused on the flow inside the snout and concluded that flow of zinc in front of strip is dominated by the flow entering the snout, caused by the rotating sink roll.

Ouellet *et al.* [14] conducted an experimental study on a 1/5 scale water model. They used Particle Image Velocimetry (PIV) technique to validate their numerical simulation results as shown in the literature. Toussaint *et al.* [15] performed an experimental study to determine the fluid flow pattern using hot visible liquid as molten zinc model.

Numerical simulations have been also widely used to model the fluid flow inside the bath. Ajersch *et al.* [16] studied the turbulent flow and temperature distribution in a galvanizing

bath through three dimensional numerical simulations. They showed that there are some regions with high temperature gradients close to the inductors and the melting ingot. Willis *et al.* [17] carried out numerical simulations for the fluid flow and temperature distribution for two certain bath geometries. They supported their hypothesis saying that the temperature distribution has to be uniform to inhibit dross formation and that flow conditions are related to intermetallic precipitation in the bath.

Willis *et al.* [18] performed a multiphase flow study using massless particle and observed the number of particles settling at the bottom of the bath increased with particle size. Pare *et al*. [19] tracked solid particles with different densities starting from center of the bath to the back of the strip. They concluded that the particle trajectory lines vary depending on the particle density and initial position they are released. Paik *et al.* [20] examined the composition difference in top and bottom dross particles. They showed that smaller particles have different composition of aluminum and iron in compared with the larger particles.

In some other studies the amount of Al and the temperature profile in the bath were studied. These parameters were measured through computer programs for bath management purposes, such as DEAL™ (Determining Effective Aluminum) and MAP™ (Modeling Aluminum Pick-up) [21].

Previous studies can be summarized as:

1. It was concluded that due to the direct contact of steel strip with the bath fluid, formation of intermetallic particles was found to be inevitable.
2. According to previous studies, the strip velocity motion determines the roll rotational velocity which affects the fluid flow behaviour close to the strip and near the sink roll.
3. It can be generally stated that, the fluid flow near the ingot region is dominated by thermal effects in the bath. Whereas at the area close to the strip and moving rolls, the flow is affected by the motion of the steel strip and sink roll.

4. It has been found that the galvanizing line speed does not change the bulk flow pattern significantly but modifies the velocity field in the snout region, near the strip and near the sink roll.
5. It was shown that dross particles become more concentrated in the “V-section” on top of the roll, between the steel strip entry and exit region. This is due to the rotation of roll with the same direction of the strip motion.
6. It was concluded that temperature gradient is one of the main reason of dross particles. Local decreases in temperature near the melting ingot will reduce the solubility of iron and aluminium. Therefore, any excess aluminium due to the temperature variation will result in increasing of dross formation.
7. It was studied that proper bath management techniques such as controlling of bath temperature can help us in minimization of the dross particle formation rate in the galvanizing bath throughout the production of high quality coatings.

2.2 Summary

The present work is aimed at advancing the understanding of dross particle agglomeration on the sink roll in a galvanizing bath. Due to the complexity of the agglomeration mechanism in the bath, particle trajectories and particle-surface interactions are modeled in this study. Therefore, the novelty of this research can be summed up as:

1. Analysing the fluid flow behaviour in the near vicinity of the roll where it meets the strip.
2. Studying the particle-surface interaction within the bath, as an important key in understanding the dross build-up on the roll surface

Chapter 3

3 Numerical Setup

In this section the governing equations for solution of the bath fluid flow and particle are presented. To achieve our goals and track the particles motion in a complex multiphase flow system, first the fluid flow has to be fully understood. Once the bath fluid flow is modeled, then solid particles can be released into the bath and coupled with the continuous phase. Particle trajectories and their collisions with the hardware components will be studied in this research. The following sections describe the governing equations in a hot-dip galvanizing bath.

3.1 Multiphase flow

Studying the dynamic behavior of multiphase (liquid–solid) flows is crucial due to its relevance to a wide range of applications in industries such as agglomeration processes, fluidized bed and dip-coating. There are two popular modeling approaches which are used for multiphase (liquid-solid) flow problems. They include macroscopic continuum-continuum approach introduced by an Eulerian-Eulerian model, and microscopic continuum-discrete approach defined by an Eulerian-Lagrangian model [22].

3.1.1 Eulerian- Lagrangian approach

In Eulerian-Lagrangian approach, the particles are defined as a discrete phase made of spherical particles dispersed in the fluid. In general, the detailed flow field is solved first, and then solid particles are released to the fluid. Particle trajectories can be determined by the integration of Newton's second law for each individual particle [23]. In the continuum-discrete approach, the fluid behavior is determined by solving the Navier-Stokes equations, whereas solid particle motion is defined using the Newton's law of motion for individual particles with their coupling of Newton's third law of motion [24]. This approach, unlike the previous one, can provide detailed information about the particles trajectories and the transient forces between the particles as well as between the particles and fluid to the extent that many such methods have been developed over the past decades.

3.2 Governing equations

The fluid flow in the galvanized bath can be defined using the Navier–Stokes equation with some assumptions. The conservation equations which can be applied in the galvanizing bath are continuity and momentum equations:

$$\nabla \cdot u = 0\,, \tag{3-1}$$

$$\rho \frac{du}{dt} = -\nabla P + \mu \nabla^2 u + \rho f\ . \tag{3-2}$$

Where ρ is the fluid density which is constant, u is fluid velocity, P is the pressure, μ is the viscosity coefficient, and f is defined as the body force per unit mass [25].

The assumptions [9] made to model the fluid flow in the bath are:

- The molten zinc flow in the bath is turbulent
- The bath liquid behaves as a Newtonian fluid
- The bath flow field is isothermal. (No temperature gradient is in the bath)
- The fluid flow is steady state
- The level of the liquid in the bath remains constant

According to the literature review mentioned in chapter 2, the fluid flow in the bath is fully turbulent. In a turbulent flow, the field properties become random functions of location and time. Velocity and pressure values can be decomposed into their mean and fluctuation values. Averaging the Navier-Stokes equation can result in a new form of equations referred as Reynolds equation [26].

$$\frac{\partial \mathrm{U_i}}{\partial \mathrm{t}} + \mathrm{U_j}\frac{\partial \mathrm{U_i}}{\partial \mathrm{x_j}} = -\frac{1}{\rho}\frac{\partial \mathrm{P}}{\partial \mathrm{x_i}} + \nu \frac{\partial^2 \mathrm{U_i}}{\partial \mathrm{x_j x_j}} - \frac{\partial \overline{\mathrm{u_i' u_j'}}}{\partial \mathrm{x_j}} \tag{3-3}$$

In this equation, $\mathrm{U_i}$ and P are the mean velocity and mean pressure respectively and $\mathrm{u_i'}$ is the velocity fluctuation component. The last term in Equation (3-3) is related to turbulent stress and sometimes called as Reynolds stress, τ_{ij}^{T}.

$$\tau_{ij}^{T} = -\rho\overline{u_i' u_j'} \tag{3-4}$$

One of the most common turbulence models that has extensively been used in numerical modeling and simulation software is k-ε model. The model is based on the assumption that Reynolds stresses are linearly related to the mean deformation [25].

$$-\rho\overline{u_i' u_j'} = \mu_T\left(\frac{\partial U_i}{\partial x_j} + \frac{\partial U_j}{\partial x_i}\right) - \frac{2}{3}k\rho\delta_{ij} \tag{3-5}$$

Here, $\mu_T = \dfrac{\rho c_\mu k^2}{\varepsilon}$ is the turbulent viscosity that defines the kinetic energy of turbulence fluctuation, k and turbulence dissipation rate, ε. Two more equations are required to be solved in terms of turbulence kinetic energy, k and turbulence dissipation, ε [25].

$$\rho\left(\frac{\partial k}{\partial t} + \boldsymbol{u}\,.\,\nabla k\right) = \nabla\,.\,\left[\left(\mu + \frac{\mu_T}{\partial k}\right)\,\nabla k\right] + P + G - \rho\varepsilon \tag{3-6}$$

$$\rho\left(\frac{\partial \varepsilon}{\partial t} + \boldsymbol{u}\,.\,\nabla \varepsilon\right) = \nabla\,.\,\left[\left(\mu + \frac{\mu_T}{\partial \varepsilon}\right)\,\nabla k\right] + C_{\varepsilon 1}\,\frac{\varepsilon}{k}\,(P+G) - C_{\varepsilon 2}\rho\frac{\varepsilon^2}{k} \tag{3-7}$$

Where P= μ_T $[(\nabla u + \nabla u^T)]$ is the shear production and G is for the effect of the buoyancy ter. $C_{\varepsilon 1}$, $C_{\varepsilon 2}$, $C_{\mu,}, \sigma_\varepsilon$ and σ_k are all the model constants which are known [27].

3.2.1 Particle Equation of motion

The particulate phase is represented by a number of computational particles whose trajectories are computed by simultaneously integrating:

$$\frac{dX_p}{dt} = U_p \tag{3-8}$$

$$\frac{dU_p}{dt} = F_D\left(U_f - U_p\right) + \frac{g(\rho_p - \rho)}{\rho_p} + F_x \tag{3-9}$$

Here U_p is the particle velocity, $F_D\left(U_f - U_p\right)$ is the drag force per unit particle mass and where F_x is an additional acceleration (force/unit particle mass) term. [29, 30]

3.3 Particle Transport Mechanisms

1- Brownian diffusion

Brownian motion can be described as random interactions of the particles. Brownian diffusion can be a dominant transport mechanism when the particle diameters are less than 0.1 μm [30, 31].

2- Turbulent diffusion

Turbulent diffusion is the collisions of particles with the turbulent structure through semi-organized pattern. The velocity fluctuations of the fluid flow influence the diffusive flux of the particles and will contribute to momentum transport in turbulent flows [32, 33].

3- Turbophoresis

This mechanism moves the particles toward the direction of lower turbulence level [30]. Caparolani *et al.* [34] studied this mechanism and concluded that turbophoresis can increase the particle deposition rate due to the high turbulence gradients.

4- Drag Force

When there is a relative motion between the solid particles and the fluid, drag force will affect the particle motion by reducing the particle speed.

$$F_D = \frac{1}{2}\,\rho C_d \mathrm{A}_p (U_f - U_p)^2 \tag{3-10}$$

U_f is the fluid velocity, U_p is the particle velocity, A_p is particle projected area and C_D is the drag force coefficient. For small Reynolds number referred as Stokes regime, the solution for the drag coefficient can be found as:

$$C_D = 24 / Re_p \tag{3-11}$$

For a transition region one of the most common correlations is:

$$C_D = 24 / Re_p \,(1 + 0.15\, Re_p{}^{0.687}) \quad \text{for} \quad Re_p<400 \tag{3-12}$$

Above Re_p=1000 in which referred to as the Newton regime, the flow is considered fully turbulent. The drag coefficient at this regime remains constant [35].

$$C_D = 0.44 \tag{3-13}$$

5- Gravitational force

Gravitational force is the resulting force due to the particle weight and buoyancy. This force in unit of particle mass can be written as: [35]

$$F_G = \frac{\rho_p - \rho_f}{\rho_p} \text{ g} \tag{3-13}$$

In this study, only drag and gravitational forces, including buoyancy are considered. Brownian force is neglected due to the size of top dross particles. Turbulent diffusion is neglected because the fluid is dilute. Since isothermal condition is assumed, thermophoretic force is not accounted for the simulation in this work.

Chapter 4

4 3-D fluid flow study in the bath

In this chapter, a fluid flow study has been performed at two different scales: general flow structure and detailed fluid flow behaviour in the near vicinity of the roll-strip.

4.1 Fluid flow studies

To study the fluid flow behavior within the galvanizing bath, computational fluid dynamics method has been used available in Ansys FLUENT. The computational domain of the galvanizing bath is described followed by boundary conditions and problem set-up.

4.2 Computational Domain

Galvanizing bath consists of a continuous steel strip which rotates around a sink roll through the snout, and two stabilizing rolls. In this study, the geometry of the bath has been selected based on an industrial galvanizing line described in the literature [18]. Different components of the galvanizing bath are shown in Figure 4-1. Some types of galvanizing baths, particular geometries of grooves are machined on the roll surface. These particular grooves prevent the sliding of the strip from the roll, which will be discussed in further chapters.

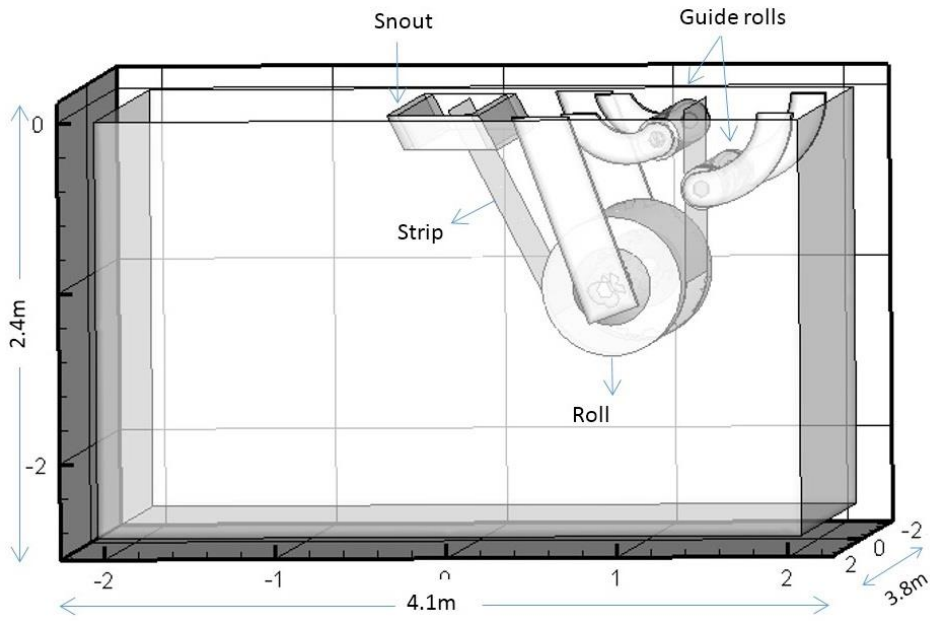

Figure 4- 1: Geometry of the studied galvanized bath

4.3 Numerical Procedure

To determine the velocity distributions in the bath CFD software, Ansys FLUENT (Version 14.5) is employed to simulate the flow.

The isothermal incompressible Navier-Stokes equations are solved using k-ε turbulent model with realizable mode for better accuracy and steady-state conditions. The convective terms in the momentum equation as well as in the k-ε equations were discretized according to second order up wind scheme.

In this study the boundary conditions have been defined based on the industrial galvanizing bath mentioned in the literature [18]. The steel strip has a velocity of 3 m/s with an angle of 27 degree. The rolls' angular velocities are defined in accordance with the strip velocity. The sink roll rotates with uniform velocity of 7.5 rad/s, and guide rollers rotate at speed of 24 rad/s. Top surface is defined as a free surface. All other surfaces are stationary walls with no slip condition. Operating and bath data are shown in Table 4-1.

Table 4- 1: Configuration and operating conditions [18]

Hardware Component	Size
Snout depth	0.2
Strip width (m)	1.5
Roller depth (m)	1
Large roll diameter (m)	0.80
Guide rollers diameter (m)	0.25
Bath height (m)	2.4
Bath width (m)	3.8
Bath length (m)	4.1
Strip entry angle (°)	27
Strip velocity (m/s)	3

4.4 Mesh Grid Generation

ICEM CFD is employed to generate the mesh for the galvanizing bath using tetrahedral elements. In ICEM CFD there are two main methods for creating volume elements depending the complexity of the computational domain. In the first method, which is usually named as blocking method, parts are defined and created in some blocks associated with the problem domain. Proper points of the domain have been created using Geometry tab, Create Point and Explicit Coordinates option. Curves are associated with the points drawn from Geometry tab. Surfaces of the block from the appropriate curves are drawn afterwards. By determining the location where the fluid is located, the fluid volume elements can be identified by populating the fluid through each block. This method of grid generation is very simple and efficient for simple geometries, especially where boundary layers on the wall are required.

As demonstrated in Figure 4-1, the galvanizing bath consists of three cylinders, a snout, pinion arms and a steel strip which is considered a complex geometry. Therefore, using blocking method for grid generation is almost impossible.

In an alternative way, lines and curves of each part are drawn properly according to the problem information. The parts where higher mesh resolution is needed are defined with

smaller surface elements. By generating the surface mesh elements, all of the bath hardware components will have their particular mesh resolution depending on where need to be studied as displayed in Figure 4-2. The last step is to populate the surface elements within the computational domain to cover it with volume elements.

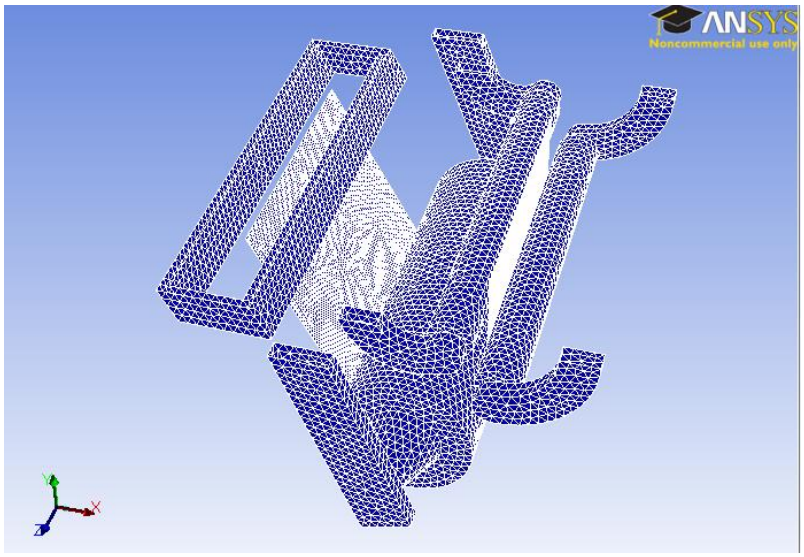

Figure 4- 2: Surface elements in the galvanizing bath

Figure 4-3 shows a cross section of surface elements at the middle of the bath using ICEM CFD. The final mesh contains approximately 1.5 million tetrahedral elements with 3 million faces.

Generally, obtaining the proper and accurate results in computational fluid dynamics studies depend on different factors such as the model, numerical scheme, discretization order and type, proper definition of boundary conditions. One of the significant parameters for obtaining accurate and correct simulation results is generating an appropriate grid.

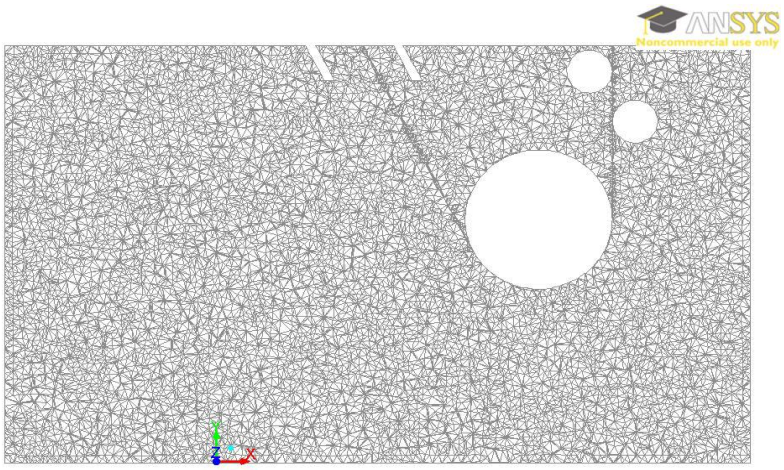

Figure 4- 3: Cross section of the initial mesh within the bath

In this study, initially a coarse mesh is generated to determine the general fluid flow structure within the bath as depicted in Figure 4-2. However, in order to analyse the fluid flow at near roll-surface, a finer mesh including high resolution volume elements is required.

One of the major challenges which adds more complexity in to the mesh generation process was to generate very fine elements with acceptable mesh quality (aspect ratio more than 30%) at the wedge area where roll and strip converge. This is because of the attachment of a flat surface to a curved surface, results in the formation of skewed (poor-quality) elements. These elements might be one of the reasons for inaccurate fluid flow solution within this area. Therefore, many efforts have been performed in order to increase the local mesh resolution of the skewed volume elements at the wedge area. This includes quality improvement by iteration method, creating high resolution surface elements on the hardware components, creating patches at the wedge area and creating prism layers.

Figure 4-4 displays high resolution surface elements on the hardware components. Tiny elements at the wedge area compared to the other larger elements far away from the roll are shown in a bath cut plane in Figure 4-2.

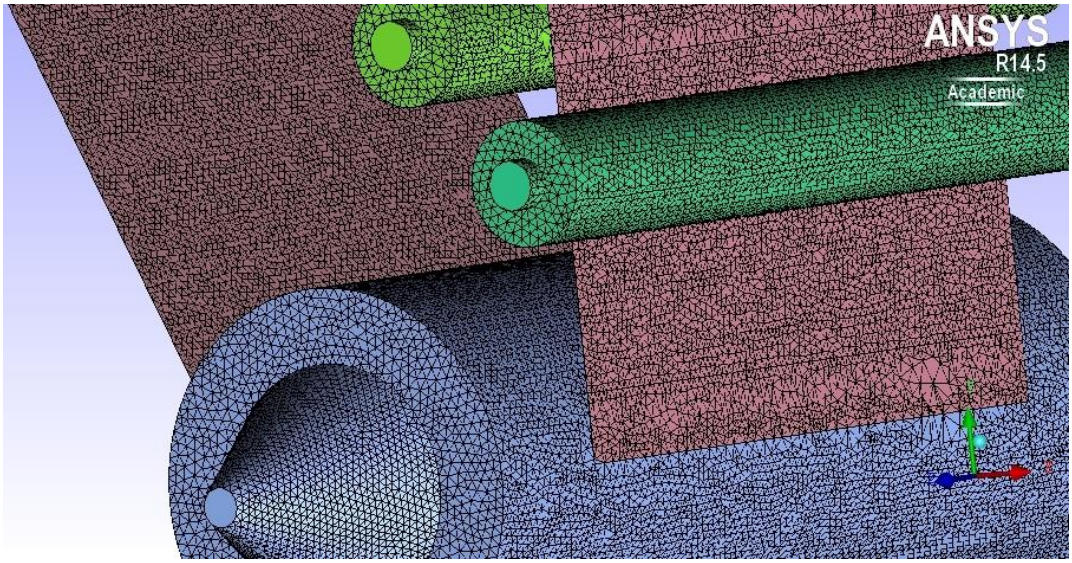

Figure 4- 4: Improved surface elements of the bath hardware components

Bath length scale issue and poor mesh quality at the wedge area are the main challenges. Bath length scale issue refers to the bath geometry scale compared to the near-roll surface scale which makes the simulation vey time costly. The other challenge is resolving the mesh resolution at the wedge is very close to the roll and strip. Figure 4-5 is a schematic view of the wedge area.

Since at the wedge area, a curved surface is attached to a flat surface, very tiny elements are required to be generated at the extreme vicinity of each roll. The local mesh quality was resolved by iterating method for minimum cell length ratio of 30%.

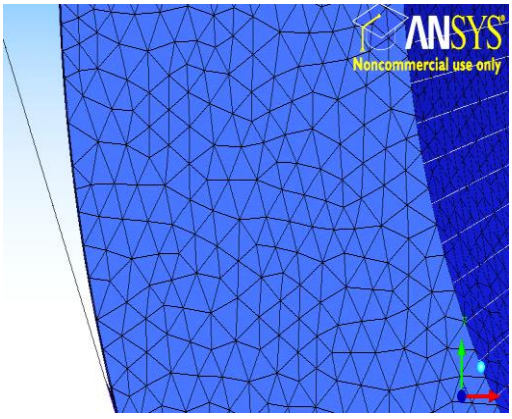

Figure 4- 5: Wedge area near the roll

To study the fluid flow pattern in the near vicinity of the roll, very fine fluid cell elements are formed around the sink. The following steps have been undertaken to generate a suitable mesh grid with a fine resolution near the roll:

1. Defining the surface mesh set-up
2. Creating tetrahedral (robust) mesh with the smoothing procedure
3. Creating Delaunay mesh along with the smoothing procedure
4. Defining prism set-up
5. Creating prism layer, smoothing the mesh
6. Improving the mesh resolution
7. Checking the mesh and exporting it to the solver

Figure 4-6 demonstrates the cross section of tiny elements around the roll surface compared to the other cells far away from the roll. A closer view of the grid is depicted in Figure 4-7. It is obvious that due to the costly calculation time, creating tiny elements in the whole domain is not necessary, especially when the study concentration is known.

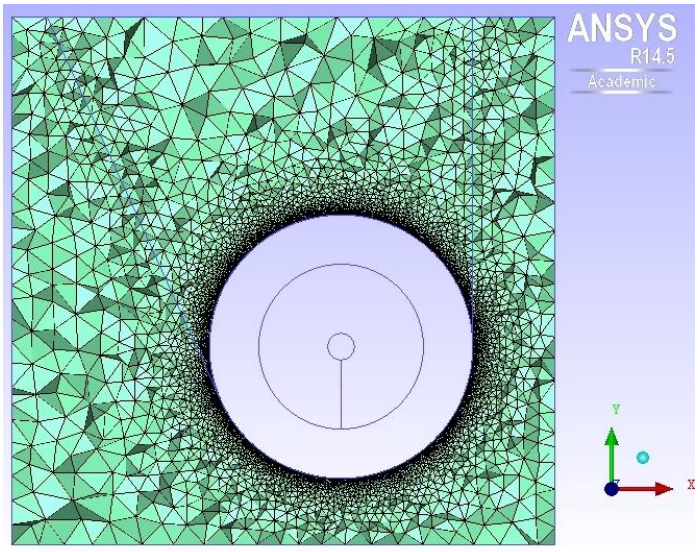

Figure 4- 6: Cross section of the mesh grid at the middle of the bath

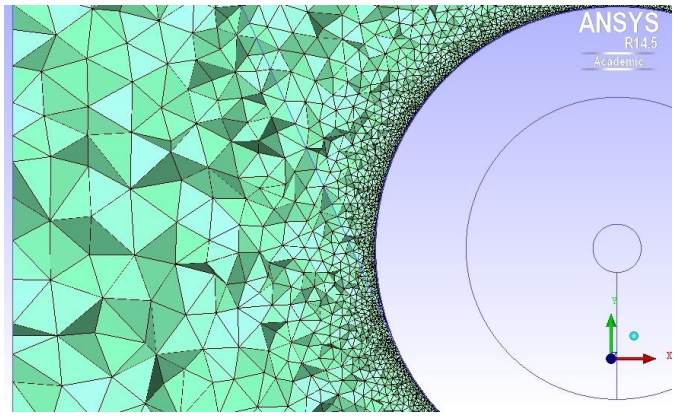

Figure 4- 7: Close-up view of the mesh grid close to the sink roll

Prism layers are also used to create a mesh with higher aspect ratio at the wedge area shown in Figure 4-8. Creating smaller surface elements or using prism layers could not totally remove the skewed elements within the area of interest. Therefore, in an innovative approach all the four areas consist of skewed elements are separated and referred to as patch areas. As displayed in Figure 4-9, these areas are filled with tiny fluid elements to reduce the mesh skewedness.

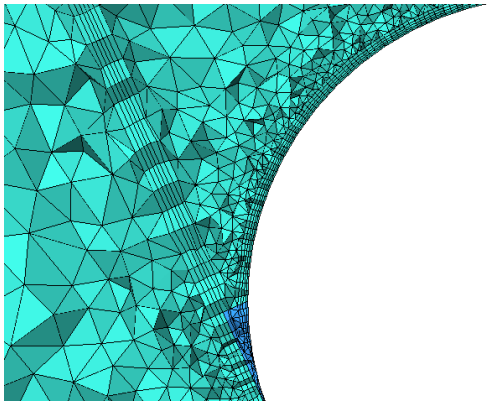

Figure 4- 8: Displaying the prism layers on the roll and strip surface

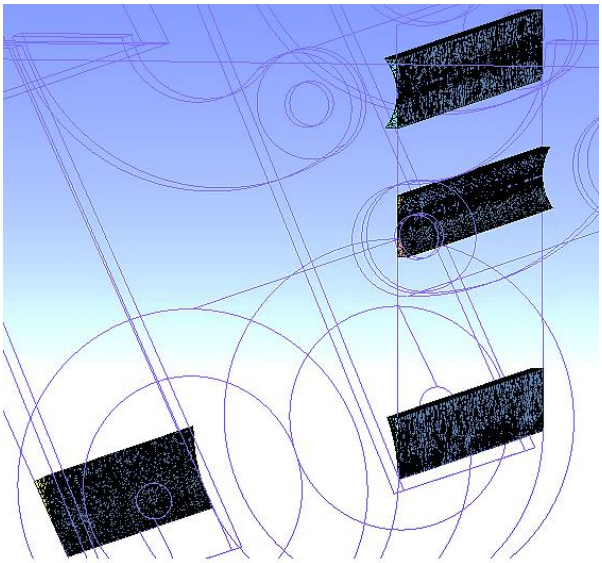

Figure 4- 9: Improvement of volume elements at the wedge area

4.5 Simulation Conditions

The dynamic behavior of the fluid inside the bath is simulated using realizable k-ε method in Ansys FLUENT. This is due to its reliability as a RANS model for free stream turbulence modeling and inexpensive computational cost [36]. The fluid property in a fixed temperature condition has been set for the simulation [37]. The simulation has been continued with the convergence rate of 1.0E-5 for the continuity, velocity components, k and ε . Constant bath fluid properties are used for the calculations at 460℃; density ρ=6600 kg/m^3 and viscosity μ=0.004 Pa.s. [38].

In this study standard wall function (SWF) has been defined for law of the wall in the modeling. Therefore, Y^+ parameter is checked to be in the valid regime which is 30<Y^+<300. Y^+ is a non-dimensional wall distance for a wall-bounded flow.

$$Y^+ = \frac{Y\, u_*}{v} \tag{4-1}$$

In this equation, u_* is the friction velocity at the nearest wall, Y is the distance to the nearest wall and v is the local kinematic viscosity of the fluid. Y^+ is often referred to simply as y plus and is commonly used in boundary layer theory and in defining the law of the wall.

Table 4- 2: Parameters used for the CFD study of liquid phase

Material	Liquid Zinc
Fluid density (kg/m^3)	6600
Fluid viscosity (kg/ms)	0.004
Fluid turbulence model	k-ε
Discretization method	Second order
Time	Steady-state
Convergence rate	1e-5
Cell type	Tetrahedral
Number of cells	1.5, 2.5 and 5M
Processing style	8 parallel processes

4.6 Bath fluid flow results

The following results are obtained from simulation of fluid flow in the galvanizing bath. Velocity contours at the middle of the bath are shown in Figure 4-10. Fluid flow behaviour within the bath at selected cross sections are depicted in Figure 4-11 and 12.

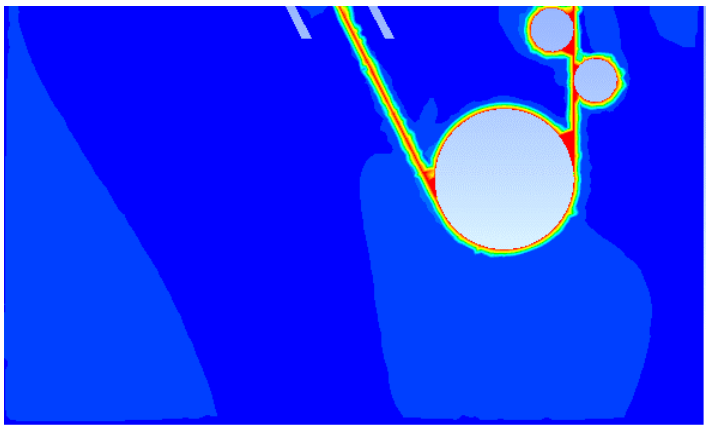

Figure 4- 10: Velocity contours inside the galvanizing bath

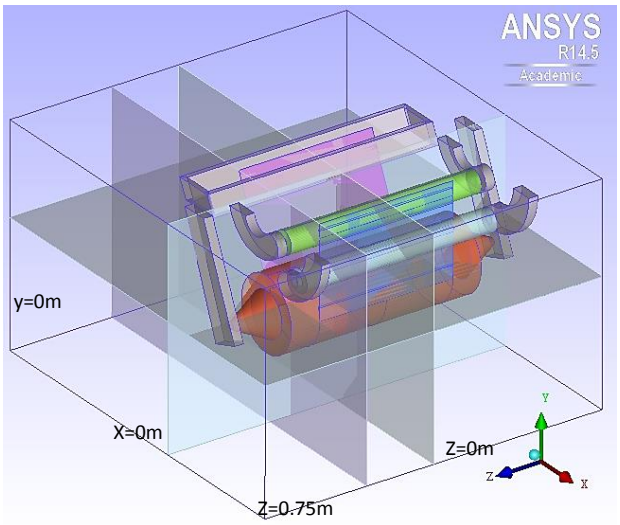

Figure 4- 11: Displaying of the cut-planes in the bath

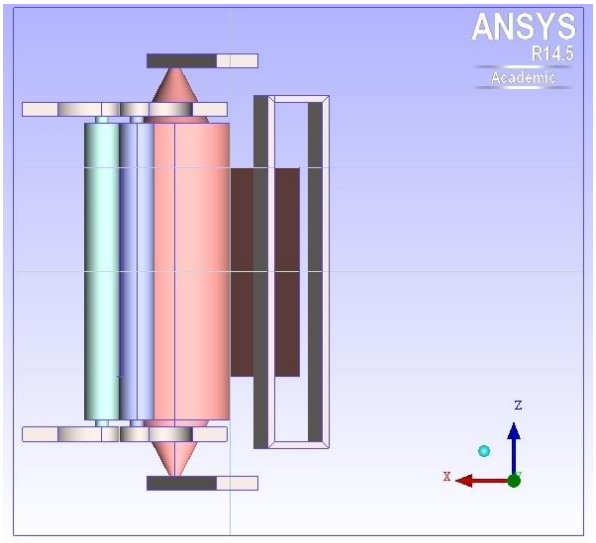

Figure 4- 12: Top view of the defined cut-planes in the bath

Figure 4-13 displays the velocity vectors at the mid plane of the bath (Z=0). The rotation of the rolls and submerging the strip down to the bath create a vortex at the top of the sink roll, which conforms to the literature.

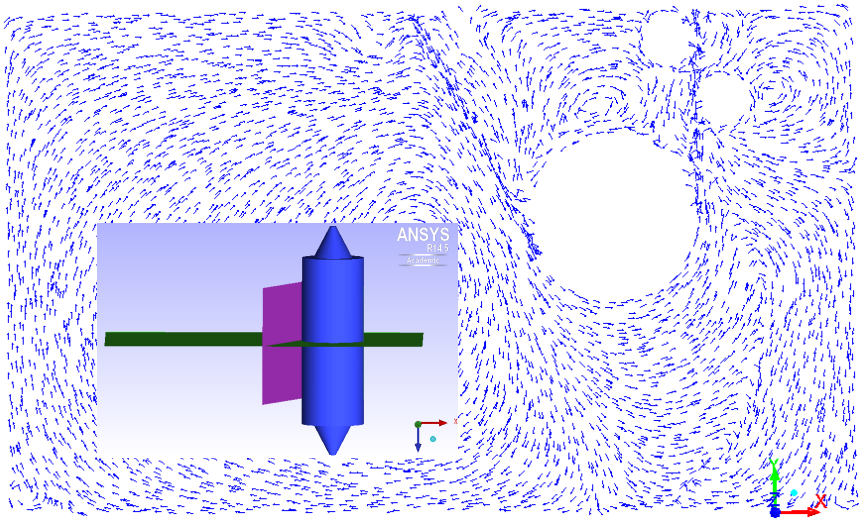

Figure 4- 13: Velocity vectors at the middle of the bath

According to the bath water model experiments performed by Gagné *et al.* [11] and numerical simulations conducted by Ilinca *et al.* [16], the fluid flow pattern structure shows a good agreement.

Ouellet's [14] numerical study, which was validated by PIV experimental method discussed in chapter 3, also conforms to the obtained simulations results from the 3-D bath model in the vortex formed on top of the sink roll at the center line of the galvanizing bath.

Figure 4-14 shows the velocity vectors at the *X-Z* plane, where it cuts the sink roll from the center. The flow structure is symmetric as expected. It displays two vortices on each side of the roll near the steel strip. Velocity contours at this plane also depicted in Figure 4-15, which indicate the velocity gradient at the strip-roll area. A better view of the velocity vectors is demonstrated in Figure 4-16. It shows how fluid flow inside the wedge area toward the roll ends and eventually leaving from the strip region.

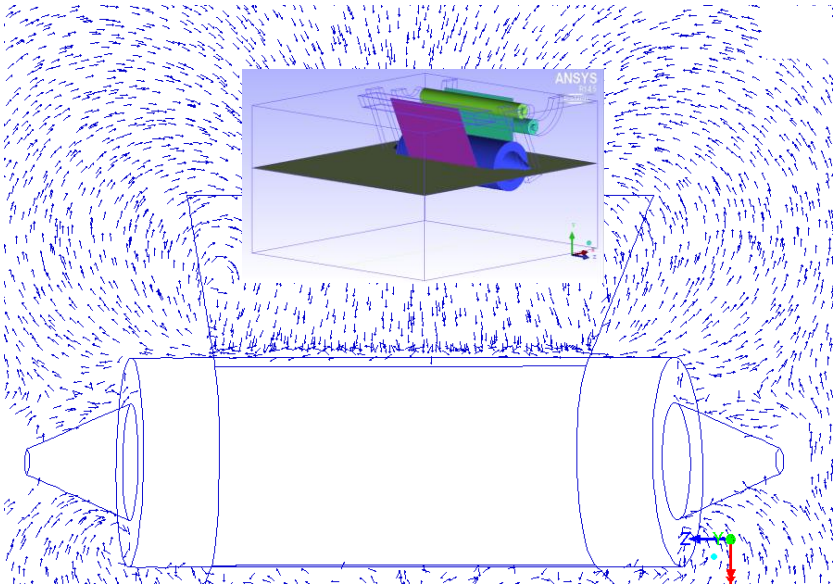

Figure 4- 14: Velocity vectors at the *X-Z* cut-plane (y=0)

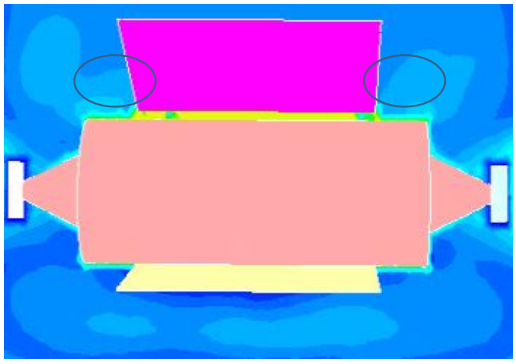

Figure 4- 15: Velocity contours at the *X-Z* cut-plane (y=0)

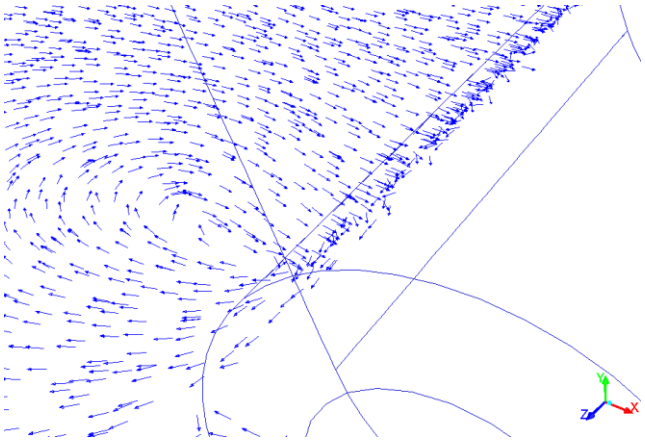

Figure 4- 16: A close-view of the velocity vectors at the *X-Z* cut-plane

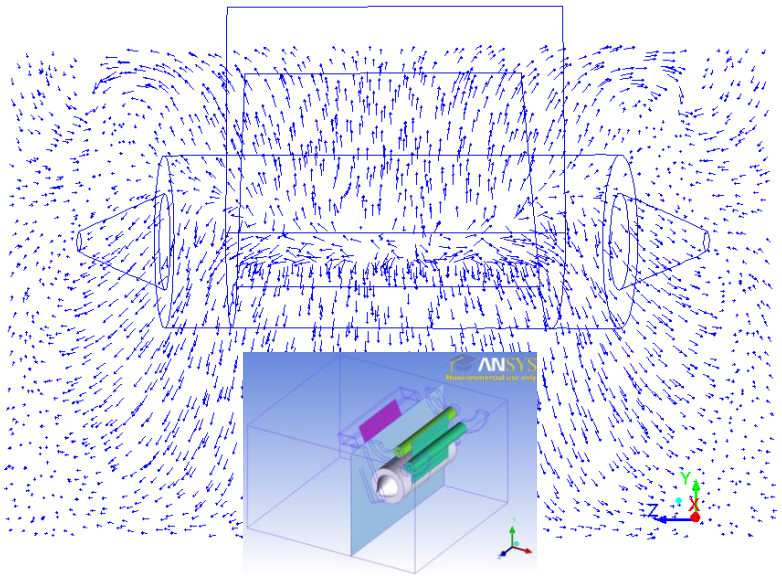

Figure 4- 17: Velocity vectors at the *Y-Z* cut-plane

Figure 4-17 displays the velocity field at the wedge area. It can be seen that the zinc fluid becomes trapped by the moving converging surfaces and then is pushed out into the open area along the roll in *Y-Z* plane where the strip ends.

The reason that the fluid is being pushed out toward both ends is that there are two converging surfaces moving in the same direction. According to the no-slip condition that was defined for walls, the fluid on each wall will have the same velocity as the walls. Since the moving strip and roll converge, the fluid will have different flow patterns as it travels away from the roll symmetry line. The zinc fluid is then pushed out from the roll center to strip edges, where it can flow freely. (Note: the width of the strip is less than the sink roll.)

The velocity vectors on the steel strip are shown in Figure 4-18. It displays the direction changing of the velocity vectors where it reaches the strip edge. Figure 4-19, the fluid flow is depicted in a 3-D view of the roll. Velocity vectors in Figure 4-18 depict how the fluid flows on the moving strip. Figure 4-19 shows that the flow with higher velocity is located at the extreme vicinity of the roll and strip end.

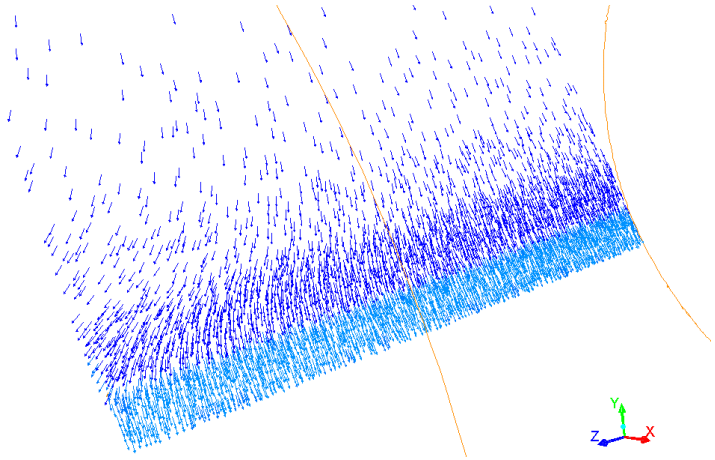

Figure 4- 18: Velocity vectors on the strip

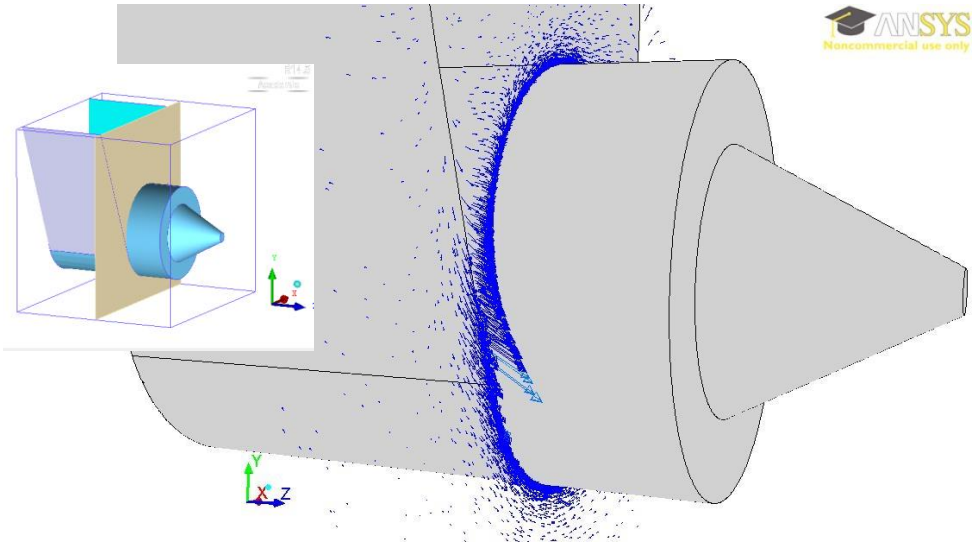

Figure 4- 19: Fluid flow direction at the wedge area

4.7 Particle-surface study

Based on the reports form industries, suspended dross particles in hot-dip galvanizing bath, can interact with the surface of the moving roll and eventually accumulate on it. To understand how dross particle interact with the hardware components, it is important to elaborate on tracking of dross particles in an industrial galvanizing bath.

This study examines particle-surface interactions near the sink roll surface in a galvanizing bath using computational fluid dynamics. The bath fluid is studied using multiphase liquid-

solid models. Particle trajectories has been studied for better understanding of our project objective which is the particle build-up mechanism on the roll surface. It is based on the hypothesis that particles agglomerate at the same location as they collide with the roll surface in the bath. The advantages and drawbacks of different multiphase models will be briefly described.

4.8 Previous studies

Numerical simulations can help us in better understanding of the fluid flow and in improving the knowledge of dross particle tracking in a galvanizing bath. Some methods have been proposed to remove the agglomerated bottom dross from the bath [39]. Fundamental fluid flow studies in a galvanizing bath have been carried out by different researchers [40].

It is evident from the previous study that the 3-D fluid flow in the bath becomes concentrated near the sink roll, where it meets the strip. This is significant because it addresses the dross particle interaction locations on the roll, where the particles most likely agglomerate on the roll surface.

Tracking of massless particles is studied in an experimental work performed by Willis *et al.* [17,18]. They observed number of particles settle at the bottom of the bath increased with particle size. Pare *et al.* [19] tracked particles with different densities at different locations: starting from center of the bath and back of strip. They found that the particle path lines depend on their densities and the initial position they are released. Kurobe *et al.* [41] used polystyrene particles and NaCl aqueous solutions to model dross and bath liquid, results showed that the particles become concentrated on top of the moving roll, where the strip enters and exits. In another study, the behavior of dross particles are examined by Gagné *et al.* [11] in a half scale galvanizing bath model. They observed the trajectories of polymeric particles with a video camera to determine the fluid flow pattern in the bath.

In some numerical studies, different multiphase models have been used to simulate the particle trajectories in several studies. In a study by Ibsen *et al.* [42], different multiphase flow models are compared with the experiment data. They concluded that the discrete

phase model is in a better agreement with the experimental observations, compared to the simulation results of continuum-continuum approach. Chu *et al.* [43] reported a detailed comparison of Eulerian-Eulerian model with discrete particle model for a fluidized bed. Rosato *et al.* [44] proposed a method for particles tracking such a way that particles are displaced step-wise. Then the fluid effect is studied through the computational domain.

4.9 Mathematical Models

There are two popular modeling approaches used for multiphase (liquid-solid) flow problems. They include macroscopic continuum-continuum approach introduced by Eulerian-Eulerian model which focuses on the behavior of bulk fluid flow and microscopic continuum–discrete approach defined by Eulerian-Lagrangian model [45].

4.9.1 Eulerian-Eulerian Approach

This approach treats both solid and liquid phases as a continuum. The method is relatively fast, since it requires less numerical computations compared to continuum-discrete approach [45]. In this approach, general behavior of the fluid phase is detailed and the detail information of the solid phase is not considered .Consequently, dilute multiphase flows consisting of small numbers of particles cannot be modeled using this approach. According to the nature of the current study, the Eulerian-Lagrangian approach is of main interest and will be discussed in the following sections.

4.9.2 Eulerian-Lagrangian Approach

In the continuum-discrete approach, the fluid behavior is determined by solving the Navier-Stokes equations, whereas the solid particle motion is defined using Newton's law of motion for individual particles with their coupling of Newton's third law of motion. This approach, can provide detailed information about the particles trajectories and the transient particle- particle and particle-fluid forces [45,46]. Many such methods have been developed over the past decades that can be divided into two models: Discrete Phase Model (DPM) and Discrete Element Method (DEM).

The main advantage of DPM model is the fast computational time, since it does not consider the collision effect that might be significant in some multiphase flows and mixing processes.

In the present work, the details of DPM and DEM multiphase models are briefly elaborated. For particle modeling, coupling of liquid with the particles is presented for three different cases: DPM for massless particles, DPM for particles with mass and DEM for particles with mass.

To simulate the particle trajectories in a galvanizing bath, there is no need to develop new codes for these complex models, since they are validated and available in CFD modeling software such as Ansys FLUENT, EDEM or OpenFOAM. Developing complex multi-scale geometry with turbulent multiphase flow is very time consuming. Thus, Ansys FLUENT has been employed as a platform. This model is extended using a DEM solver, incorporating a User Defined Function code to evaluate the particle-surface interactions and quantify the presence of particles in the extreme vicinities of the moving roll.

4.10 CFD Modeling

The liquid and fluid phase modeling is described in the following sections.

4.10.1 Liquid phase modeling

The continuum fluid phase in the presence of a secondary particulate phase is solved for each computational cell from the continuity and modified Navier-Stokes equations as shown in equations 4-1 and 4-2. [43].

$$\frac{\partial(\varepsilon_f)}{\partial t} + \nabla.\left(\varepsilon_f u_f\right) = 0 \tag{4-1}$$

$$\frac{\partial(\rho_f \varepsilon_f u_f)}{\partial t} + \nabla.\left(\rho_f \varepsilon_f u_f u_f\right) = -\varepsilon_f \nabla p - F_f^p + \varepsilon_f \nabla.\tau + \rho_f \varepsilon_f g \tag{4-2}$$

Where ε_f is the volume fraction occupied by the fluid, ρ_f is the fluid density, $\boldsymbol{uf}$ is the fluid velocity, τ is the stress tensor for the fluid phase F_f^p is the particle-fluid interaction,

force which represents the particle drag force, the pressure gradient force, and the viscous force.

4.10.2 Particulate Modeling

In this work, two different multiphase models including Discrete Phase Model (CFD-DPM) and Discrete Element Method (CFD-DEM) are employed to study particle motion near the moving surfaces.

It is clear that due to the fluid and particle-particle interactions and particle-particle interactions, simulation of the hydrodynamic of liquid–solid flow is quite complex. However, many efforts with the development of advanced computational techniques and high speed processors have been made, in order to study the complex multiphase flows including high density mesh grid and steady/unsteady discrete phase motion. These models are mainly achieved by coupling the discrete phase model (DPM) for solid phase with computational fluid dynamics (CFD) for fluid phase known as CFD-DPM. In this model the detailed dynamic behavior for both phases and forces of particles are still unknown [45]. Therefore the new approach, known as CFD-DEM approach, is proposed to understand the physics of liquid–solid flows. Both DPM and DEM models are continuum-discrete approaches which use Lagrangian particle tracking. This work studies the two different multiphase models CFD-DPM and CFD-DEM to understand particle motion near the moving surfaces.

4.11 Discrete Phase Modeling

Lagrangian particle tracking is based on a translational force balance that is defined for an individual solid particle. Each particle represents a parcel of particles which is subject to gravity, drag force, buoyancy. DPM capabilities allow us to simulate the particle motion without considering the particle-particle collision effects. Therefore, if the particle-particle or particle-wall collisions are insignificant, this method can be employed to simulate the particle behavior in the multiphase flow. Because of the assumptions and simplifications, DPM approach is valid only for dilute multiphase flows [47].

4.12 Discrete Element Modeling

DEM is a time-driven particle modeling approach which first proposed by Cundall and Strack [48]. The applications of the DEM approach vary depending on the flow geometry, the accounting of forces acting on each particle and in the method of coupling between the discrete and liquid phase. Coupling of CFD with DEM can provide detailed information about particles trajectories by solving system of N-Lagrangian equation of motion for each particle as given in equation 4-3.

$$M\frac{dv}{dt} = F_{total} \tag{4-3}$$

M is a matrix of particle mass, v is a y vector of the interacting particles and F_{total} is a sum of the forces such as hydrodynamic (gravitational, drag and buoyant) terms and non-hydrodynamic (cohesive, colloidal and electrostatic and van-der-Waals) [49]. The main disadvantage of DEM approach is its high computational time to solve the full matrix for the transient solutions related to each particle.

After computing the total force acting on each particle, Newton's equation of motion can be integrated numerically to determine the particle velocity and integrating again, the position of all particles at the current time will be known as shown in equations 4-4 and 4-5 [45].

$$m\frac{dv_i}{dt} = \sum_j^N (F_{c,ij}^p + F_{g,i} + F_{f,i}^p) \tag{4-4}$$

$$I_i\frac{d\omega_i}{dt} = \sum_j^N (T_{i,j}^p) \tag{4-5}$$

Where m_i, I_i, v_i and ω_i are the mass, moment of inertia, translational and rotational velocity of particle i. The forces are: gravitational force $F_{g,i}$, contact forces $F_{c,ij}^p$, $F_{f,i}^p$ is the particle-fluid interaction force and $T_{i,j}^p$ is the torque between particle i and j. Due to the nature of the present work and relatively large particles, non-direct contact forces such as Brownian force, van der Waals force and electrostatic force are ignored.

4.13 Collision Modeling

Collision force can affect the interaction between the particles and between particles and walls. The collision force is calculated based on a soft-sphere method using DEM which allows the particle to overlap, during collisions normally less than 0.5% of the particle diameter [50]. This overlap is used to calculate elastic, plastic and frictional forces between particles [48]. Very small time step are required to achieve precise information at each collisions which will lead to high computational time. Many efforts have been carried out to reduce the computational time by simplifying these models. However, the most common linear model is the linear spring–dashpot model which was proposed by Cundall and Strack [48]. In this collision model, spring represents the elastic deformation while dashpot accounts for the viscous dissipation.

Particle collisions are modeled using Hertzian contact model [51]. The collision force has a normal and a tangential component in which the normal force acts in a direction connecting the center of particles and is defined as:

$$F = k\delta_n^{3/2} + c_n \dot{\delta}_n \tag{4-5}$$

A linear normal damping force is also assumed in this work [36]. The linear spring-dashpot model is used for the tangential component of collision force.

$$F_t = \min(k_t\delta_t + c_t \dot{\delta}_t, \mu_s \mid F_N \mid) \tag{4-6}$$

K_t and C_t are the tangential spring and dashpot coefficients, μ_s is the static coefficient of friction. δ_i is the overlap between particles in contact in normal (n) and tangential (t) directions. Tsuji *et al.* [52] assumed that tangential dissipation coefficient is in the same order of magnitude as the normal damping coefficient $C_t = C_n$. In this work the tangential damping coefficient is assumed similar to the normal one.

4.14 Coupling between the phases and time step size

To accounting for interaction effects, four-way coupling between the two phases is required which is computationally expensive and sometimes risky to converge. Fluid affects the

particles and particles affect the fluid in addition to the effects of particle-particle collisions [48]. CFD-DEM runs the CFD and DEM solvers either simultaneously or in consecutively with the interval of usually 50-100 time-steps. Time-step for DEM needs to be extremely small to capture the inter-particle collisions than the time-step for CFD. Therefore, DEM solver has to run several time steps before transferring the solid particle data to CFD solver.

The coupling is numerically achieved such a way that at each time step, DEM will provide the solid phase information such as position and velocity for each particle. Solver uses the particle data and the volume fraction in each computational cell to update the fluid flow field by calculating the momentum exchange terms between the phases. Incorporation of the resulting forces into DEM will result in the particle motion for the next time step. Then the particle affects the fluid phase from the particles, so that Newton's third law of motion is satisfied [36].

4.15 Simulation Conditions

For the liquid phase, the dynamic behavior of the molten zinc inside the bath is already simulated. Realizable k-ε method is used due to its reliability as a RANS model for free stream turbulence modeling and for being relatively computationally inexpensive.

The discrete element method is used to track particles with different concentration near the sink roll surface. Ansys FLUENT has a number of different DEM collision models available [36]. In this work, linear Hook law model, which is a combination of a contact force and a damping force was selected to calculate the normal and tangential force for both collisions. The contact forces due to particle-particle or particle-wall collisions are evaluated in terms of the normal and tangential coefficients of restitution Bottom dross particles are assumed as identical spheres with constant radius (100 microns) and density (7230 kg/m^3) [5]. Table 4-3 shows the parameters used in this simulation for the liquid and the solid phase in the galvanizing bath.

Table 4- 3: Parameters used for the DPM and DEM studies of solid phase

Parameter	DPM	DEM
Particle Shape (m)	Sphere	Sphere
Particle Size (μm)	100	100
Particle Density $(kg/m\text{^}3)$	7230	7230
Number of Particles	1, 200 and 1000	200 and 1000
Particle Type	Massless/ Inert	Inert
Injection Location	In front of the strip and on top of the roll	In front of the strip and on top of the roll
Particle-particle Collision	Particle-particle Collison is Neglected	Overlap- Soft-sphere
Dynamic Friction Coefficient	0.25 m	0.25 m
Interaction with the Fluid Phase	1-way	4-way
Application	Dilute particle flows	Dilute/Dense flows
Normal Coefficients of Restitution	-	0.9
Coefficient of Dynamic Friction	-	0.3
Solid Phase Time Step (s)	-	1e-5

4.16 Particle-surface study results

As shown previously, it is evident that there is an insignificant influence of the moving hardware on fluid flow in the bulk of the zinc bath. However, further studies of the V-section showed the fluid tendency to move from the center of the roll toward its both ends.

To simulate the particle-fluid modeling and study the particle motion in the galvanizing bath, particles are required to be injected from a specified location. According to the literature, the main place where the particles are generated is in the snout region. However, in this work for better understanding dross particles are released (linear uniform injection) from two different locations: snout region 10mm away from the strip entrance and 10mm from the top of the roll far away from the strip as depicted in Figure 4-20.

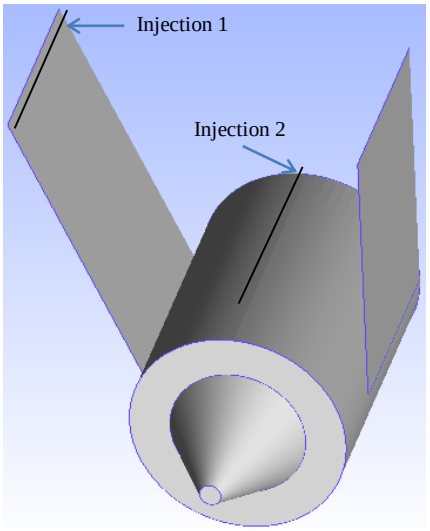

Figure 4- 20: Locations for particle injections in the galvanizing bath

Figures 4-21 and 4-22 display the particle trajectories obtained from DEM simulation for injection 1 and injection 2. It is observed that the released particles are dragged to the bath due to the strip high velocity motion. It can be concluded that particles with mass released from different locations follow the bulk fluid flow inside the bath. It was discovered that dross particles starting from the snout region remain in the V-section and move toward the sink roll top surface. This is due to the small difference in densities (9%) of the bath fluid and dross particle. The circulating motion of fluid in this region moves the dross particles toward the top surface of sink roll.

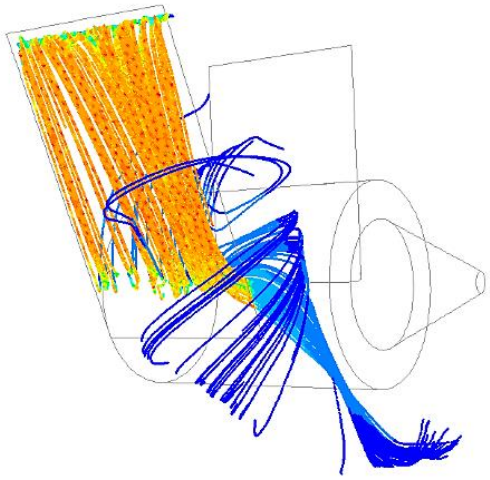

Figure 4- 21: Injection 1- From snout region in front of the strip

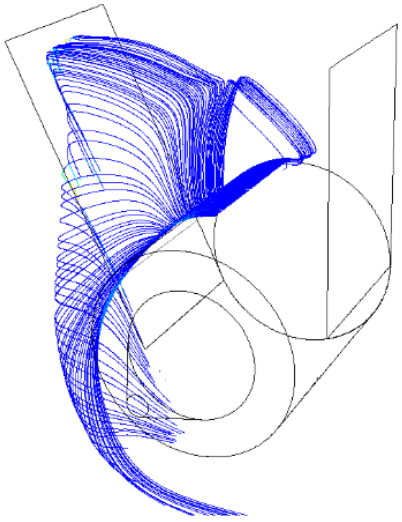

Figure 4- 22: Injection 2-From top of the sink roll

For better understanding of the particle trajectories in DPM simulation, single particles are tracked at different locations at the snout region. The following results are obtained from single particle motion at three certain locations at the strip entrance: very close to the center of the roll, middle of the strip and at the strip edge.

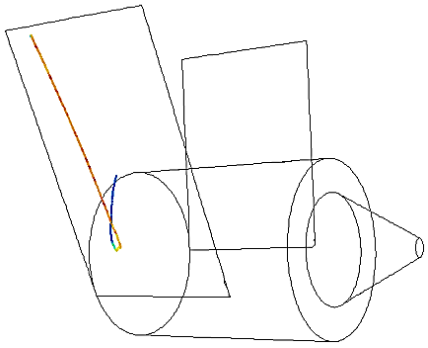

Figure 4- 23: DPM Particle trajectory for a particle close to the middle of the roll

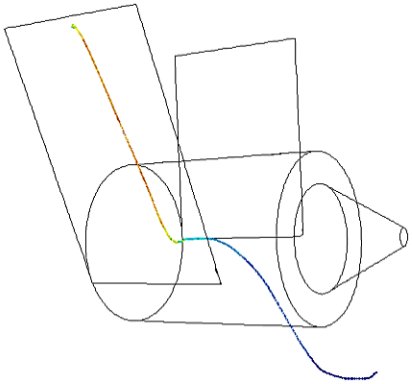

Figure 4- 24: DPM Particle trajectory for a particle closer to strip edge

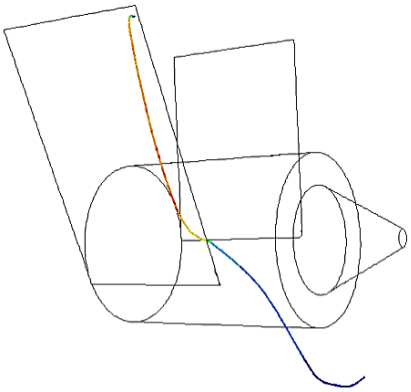

Figure 4- 25: DPM Particle trajectory for single particle released from strip edge

The same condition is repeated for massless particle at three locations near the strip-roll.

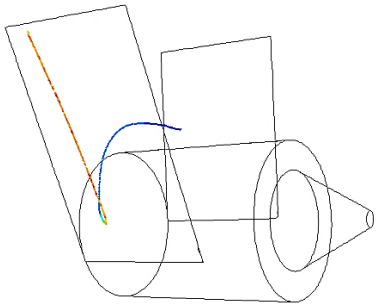

Figure 4- 26: DPM massless-particle trajectory at middle of the roll

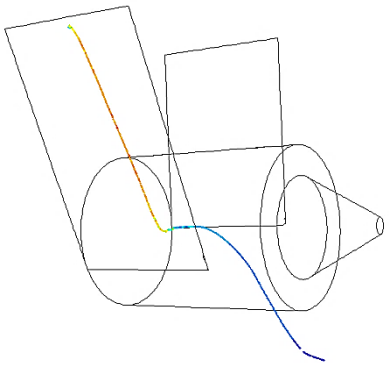

Figure 4- 27: DPM massless particle trajectory for a particle closer to the strip edge

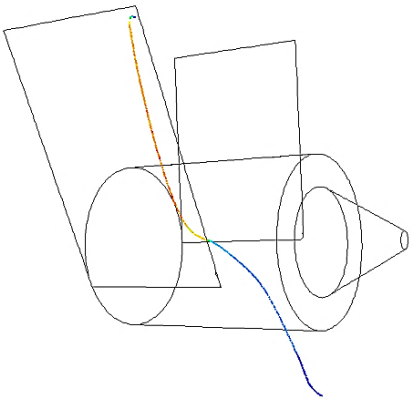

Figure 4- 28: DPM massless particle trajectory for a particle at the strip edge

According to the particle trajectories for a single particle in massless and with mass conditions, it is observed that depending on the location of particle, the particle trajectories vary. It can be concluded that in both cases if the generated dross is moving at the vicinity of the middle of roll (far from the strip edge), it will be reflected in the groove-less roll.

While, in the case where particle is moving near the steel strip edge, it is deviated from the V-section toward the roll ends. Results show that for the same amount of calculation time, particles-with-mass have shorter trajectories due to the drag force compared to the massless-particles. Since the roll is longer than strip, the location of particle-surface interaction could indicate whether the initial hypothesis is correct. This hypothesis indicates that the location in which particles agglomerate is the same as the location where particles collide with the roll.

To study the effect of the particle-surface and particle-particle collisions, an unsteady-state DEM simulation has been carried out for the bath. The particle trajectories are studied for 1000 particles after they are released from the top of the steel strip and completely coupled with the fluid bath. It was observed that the particles are circulating inside the bath and the particle motion pattern varies for each particle. As depicted in Figure 4-29, a very thin layer around the sink roll is defined with 0.5mm distance from the roll to study the number of particles located very close to the roll by incorporating a written UDF code. In the modified DEM model, the distance of each particle is calculated to the roll at each time-step. Figure 4-30 shows the cumulative number of particles that collided with the roll and those which are tracked in the defined layer at each time-step (0.005s). The number of the particles-that are tracked in the mentioned region and the number of particles collided with the roll-are identified at each time step. They are then added with the data obtained from the previous time step.

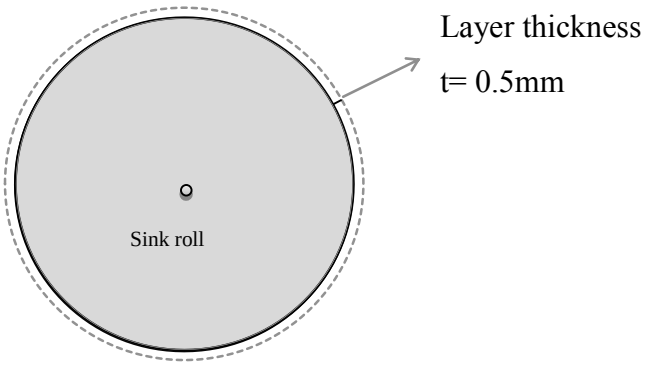

Figure 4- 29: Defined layer around the sink roll

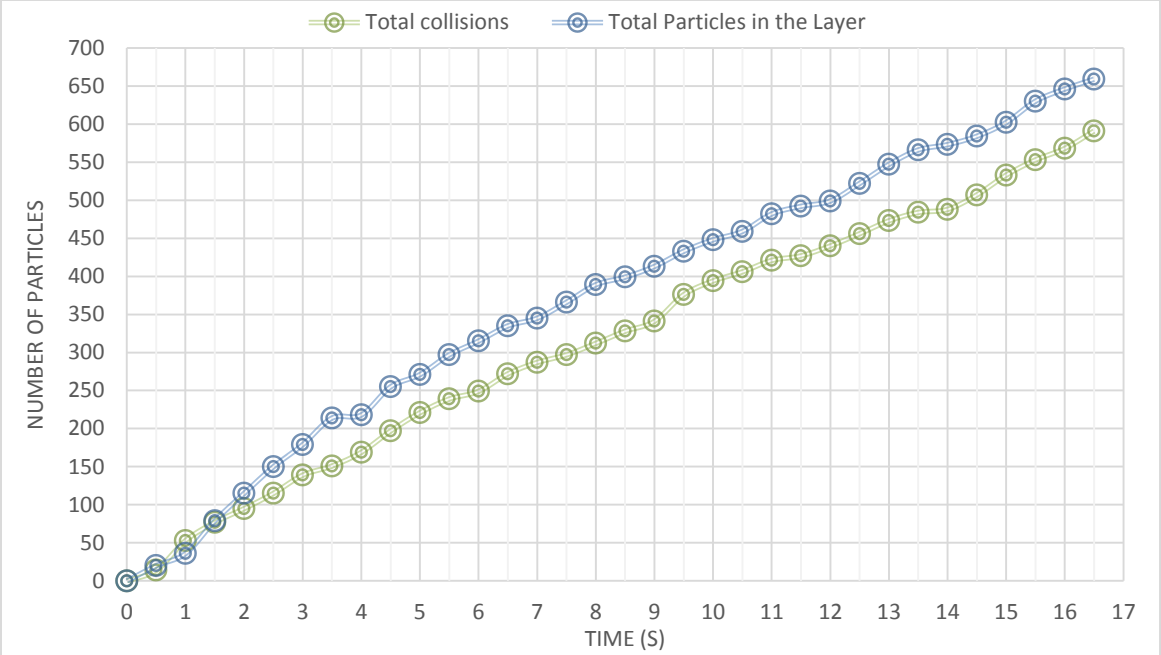

Figure 4-30: Cumulative number of particles at the extreme vicinity of the roll

4.17 Conclusions

In this work the detailed information about fluid flow in the galvanizing bath has been analysed using CFD modeling. Based on the simulation results obtained, it is concluded that the zinc fluid becomes trapped at the wedge area and then flows out the open area where the strip ends.

The 3-D liquid- solid flow inside the bath was simulated using different multiphase fluid models. Most of the injected dross particles are observed to become trapped inside the vortices in the center of V-section. The circulating motion of flow in this region drags these bottom dross particles toward the top surface of the sink roll. Findings revealed that the particle fate in the bath strongly depends on its location at the V-section region. Simulation results show that the particles generated far from the strip edge (at the vicinity of the roll centre) will remain in the V-section and move toward the sink roll top surface.

However, the particles which are initially near the strip entrance region, near the steel strip edge, are pushed out toward the roll ends due to the fluid pumping action. This resulted in the collisions of particles with the roll surface in the bath. According to reports from the

industry on the location where dross particles agglomerate on the roll, it can be concluded that the simulated results of the location of particle-surface interaction and particle agglomeration are consistent.

It was also observed that inclusion of particle-particle and particle-surface collision forces did not affect the particle trajectories significantly, since the volume fraction in this study was very small (less than 0.01%). However, at each time-step (0.005s), from the 1000 injected particles approximately 18 particles collided with the roll surface and 20 particles were tracked near the vicinity of the roll, respectively.

Chapter 5

5 Groove Geometry Study

Dross particle build-up has been reported from the galvanizing bath industries that use grooves on the roll surface. Based on an extensive literature review on the influence of the groove geometry on particle build-up, it was found that there has not been any studies on the performance of the groove in the galvanizing bath. Hence, this section is aimed at better understanding the groove performance in a galvanizing bath. To this end, a CFD simulation has been conducted for some grooves using simplified transverse fluid flow. Due to the similarity of the current research objective, a comprehensive study of groove parameter effects on hydroplaning phenomenon has been performed. Detail information is presented in Appendix.

5.1 Groove Role

In order to prevent the steel strip from slipping on the roll surface, grooves are machined on the roll surface, with different geometries and patterns. Grooves on the roll can be designed and manufactured in a spiral or radial patterns with different width, depths or spacing. A sink roll with spiral groove pattern on an industrial is studied as presented in the literature.

Grooves in the context of tires can help in expulsion of the fluid from the wedge area by providing escape channels [53-56]. There are other parameters that can affect the dross build-up phenomenon on the roll surface. These include the groove geometry of the roll and the roll hardness. In this chapter, the groove geometry effect on the fluid flow behaviour is of interest.

5.2 Groove Geometry Pattern

Various groove geometries are being used on the roll surface in galvanizing bath. Figure 5-1 demonstrates the details of three of them, selected from the industry. These grooves can be either radial or spiral on the roll with different spiral angles on the roll surface.

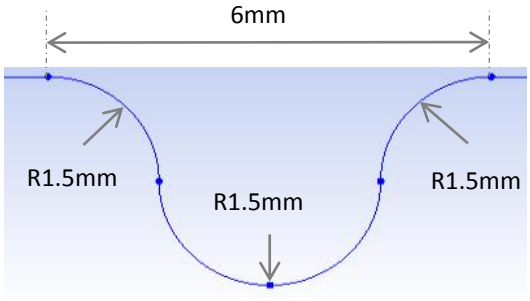

Geometry 1

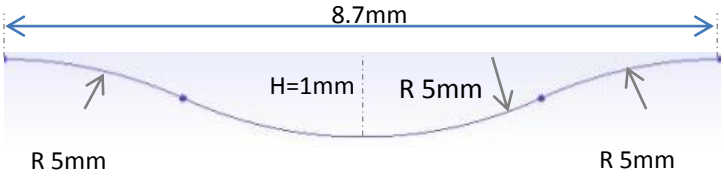

Geometry 2

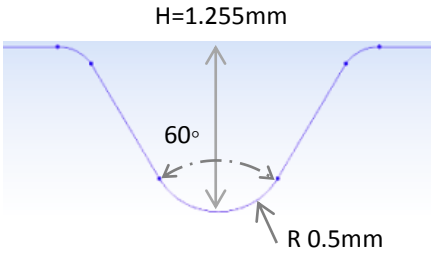

Geometry 3

Figure 5- 1: Groove geometry details

5.3 Modeling Challenges

The geometry of the zinc bath itself is too complex to study with regards to fluid flow and particle-surface interactions, with the presence of the tiny grooves on the roll surface that are immersed in the molten zinc.

One of the major challenges in this study is the length scale in the model. The galvanizing bath has dimensions of meters, whereas the roll surface groove geometries are in millimeters. In order to meet the main project objective — which is to simulate the dross particle interactions with the roll surface, including the grooves — the mesh grid has to be generated at very high density, especially within the groove channels very close to the roll. For the molten zinc fluid regions away from the roll, the mesh tetrahedral elements could gradually increase in size. An ideal mesh grid consisting of very tiny volume elements for an industrial galvanizing bath is very computationally expensive. Therefore, to examine the fluid flow behaviour on these groove geometries, a two dimensional CFD modeling has been conducted using transverse turbulent flow.

5.4 Modeling of Roll Groove Surface

ICEM software was employed in order to generate three different mesh grids as shown in Figure 5-2. For more accurate solution, the grid resolution is increased near the surface.

5.5 Problem set-up

Based on the simulation results from the 3-D bath study in chapter 4, it was concluded that pumping action moves the fluid toward both roll ends. To model this flow, a turbulent transverse flow is studied over the mentioned groove patterns with the known boundary conditions. According to the data from the 3-D bath model, a constant velocity of 0.1 m/s with k–ε turbulent model is used for each geometry surface.

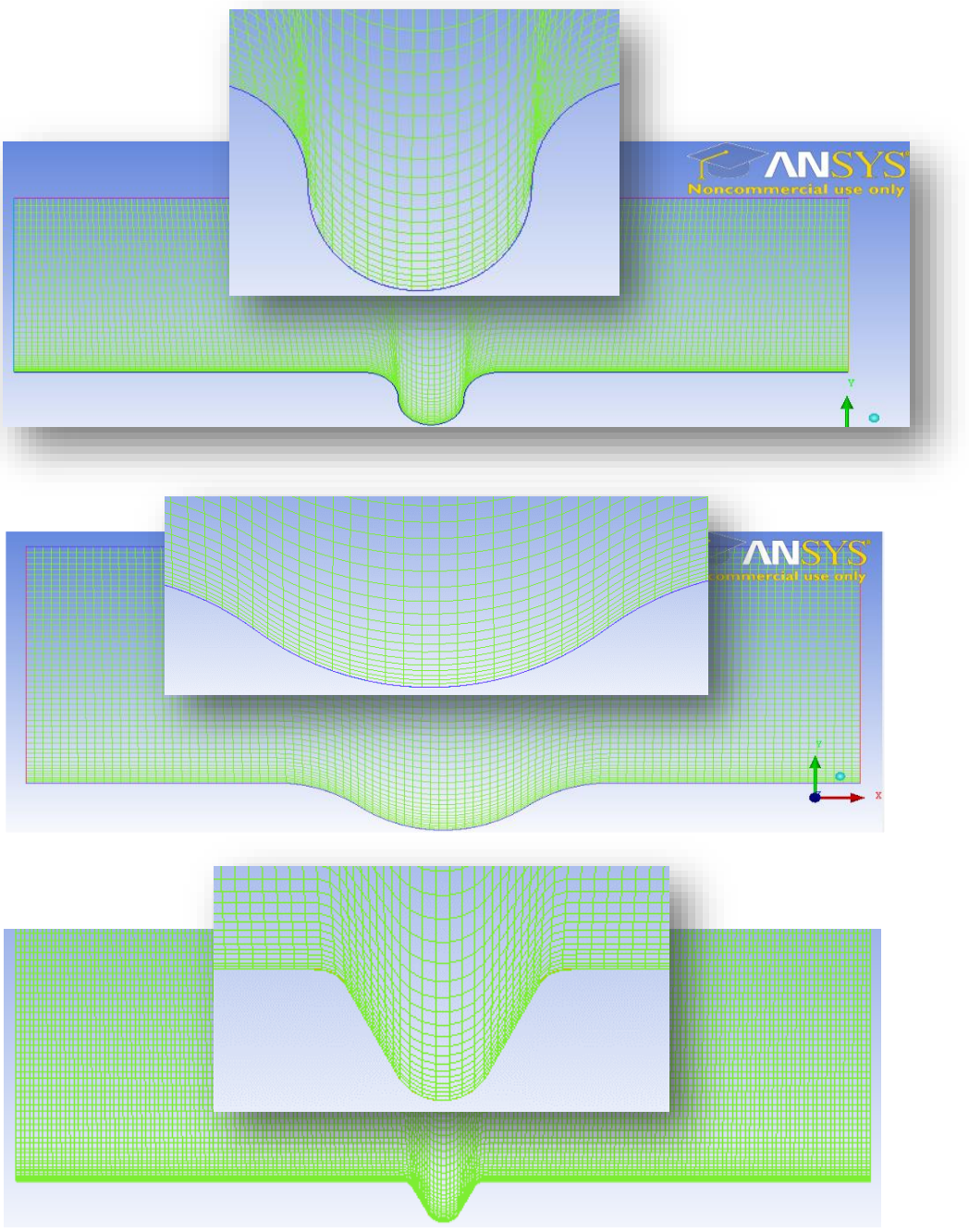

Figure 5- 2: Mesh grid for geometry 1, 2 and 3, from top to bottom

Table 5- 1: Boundary types and conditions data

Part	Boundary Type	Boundary Conditions	Turbulent Specification Method
Inlet	Velocity Inlet	$V_x = 0.1$ m/s	Turbulent intensity= 10% Hydraulic diameter= 10mm
Outlet	Pressure outlet	Gauge pressure P=0 atm	Turbulent intensity= 10% Hydraulic diameter= 10mm
Groove	Wall	No slip condition Fixed ($v = 0$)	N/A
Top surface	Moving- free surface	No gradient in Y-direction	N/A

5.6 Results and discussion

The simulation results of fluid flow, with the constant velocity inlet of V = 0.1 m/s for each groove, are shown in Figure 5-3, 5-4 and 5-5. Due to the different groove geometries, different flow fields inside each groove are observed in the profiles on the pictures on the right. It can be concluded that the flow patterns are similar in geometries 1 and 3. Stream function graphs also show the flow circulation inside grooves 1 and 3. These pictures show that, in geometry 2, the fluid can smoothly penetrate into the groove, so there is no vortex inside the groove. In another parametric study, the effect of the inlet height and inlet velocity on flow profile in each grooved surface are studied. However, these latter parameters did not change the flow field in the groove geometries.

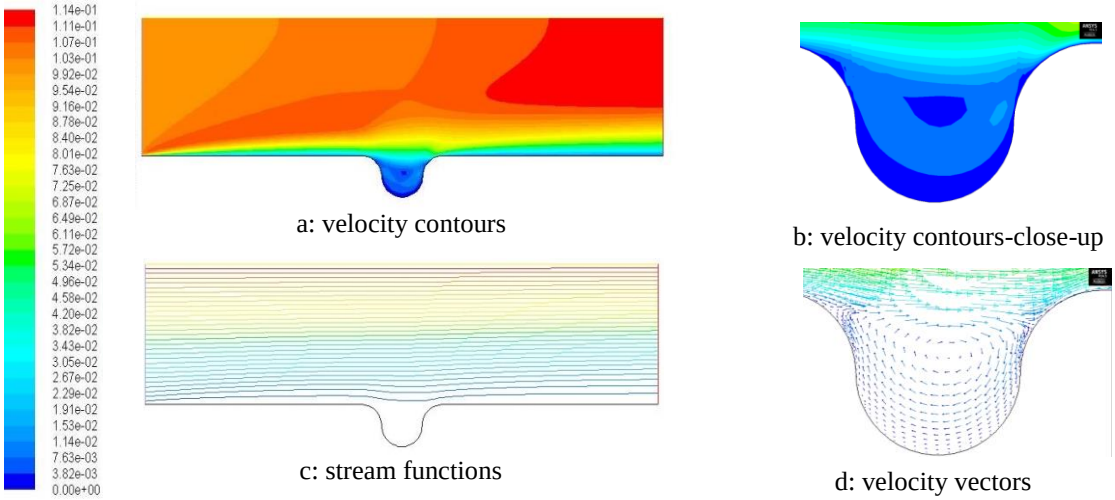

a: velocity contours

b: velocity contours-close-up

c: stream functions

d: velocity vectors

Figure 5- 3: Flow path and velocity profile in geometry 1

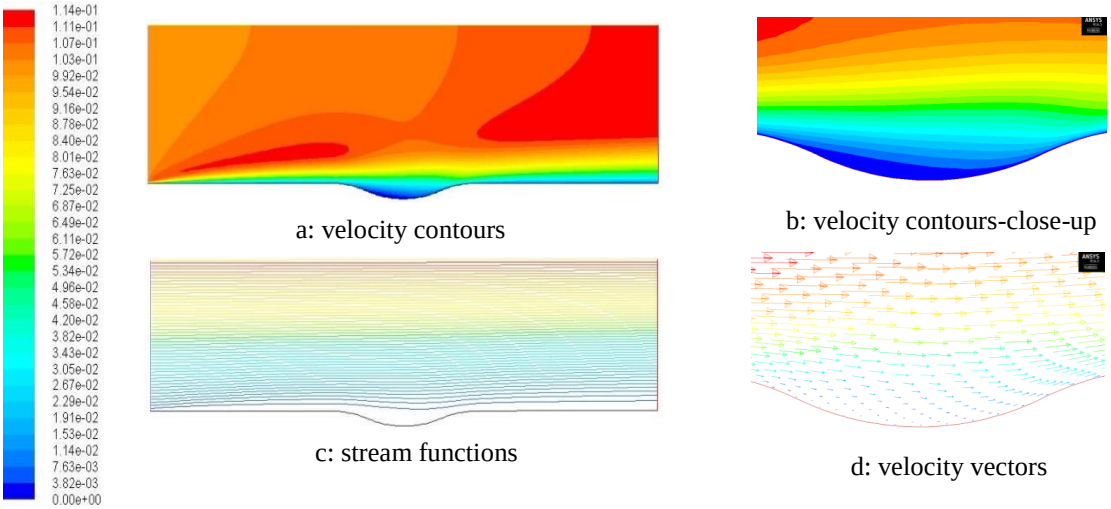

a: velocity contours

b: velocity contours-close-up

c: stream functions

d: velocity vectors

Figure 5- 4: Flow path and velocity profile in geometry 2

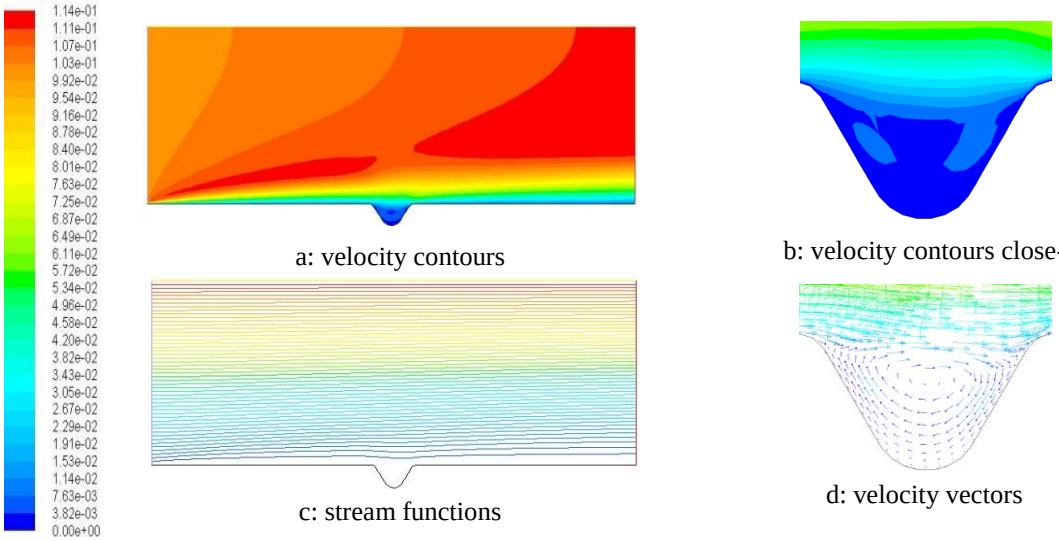

a: velocity contours

b: velocity contours close-up

c: stream functions

d: velocity vectors

Figure 5- 5: Flow path and velocity profile in geometry 3

5.7 Near- roll study

The flow profile near the roll plays an important role in dross particle interaction with the roll surface. Comparing the scale of the groove geometry of the roll surface with the size of bath, it can be concluded that determining the flow field very close to the roll requires further studies.

Fluid flow near the nip region of the roll and strip can be approximated as a fluid flow very close to a stationary block and a moving strip. In this case, the moving strip on top of the block creates a drag flow which resembles the flow passing over the center of the roll. Figure 5-6 shows simplified roll-strip model in relation with the fluid flow near the groove in the galvanizing bath. This objective has been studied for the case of grooveless block and grooved blocks (Figure 6-7) with different tilting angles to study the effect of the groove geometry on flow profile at the entrance of the nip region.

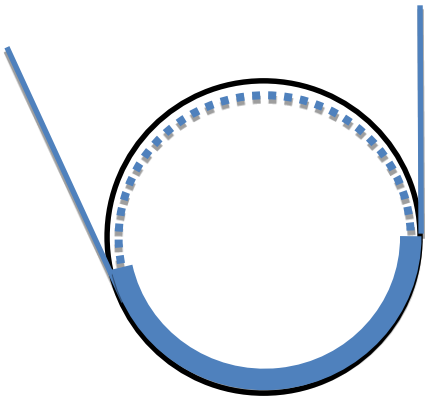

Figure 5- 6: Roll-strip models and tire-road model

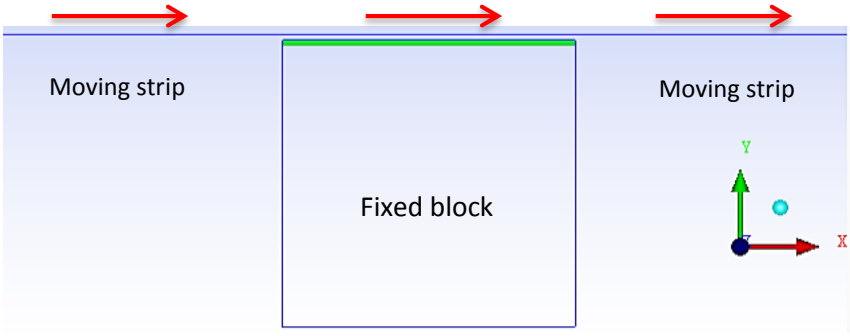

Figure 5- 7: Strip-block approximation model

5.8 Strip-Block studies- Grooveless Block

To study a simple strip-block problem without considering the groove effect on the flow field, a 2-D and 3-D geometry were studied as shown in Figure 5-8 and 5-9.

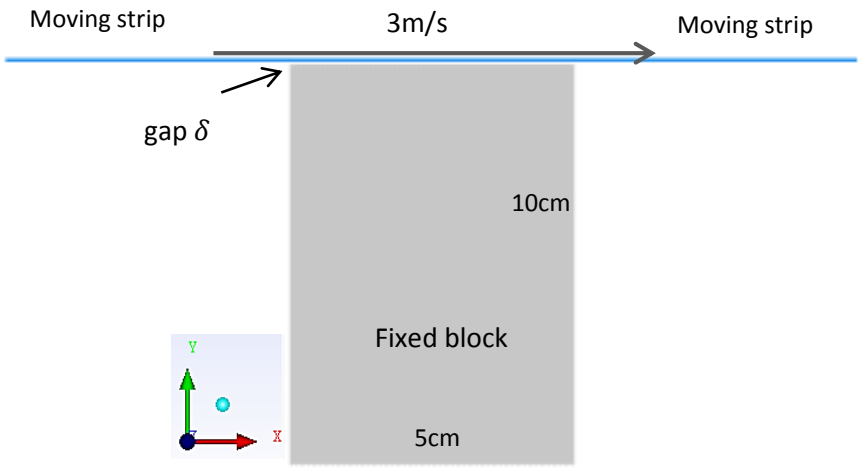

Figure 5- 8 :2-D strip-block geometry

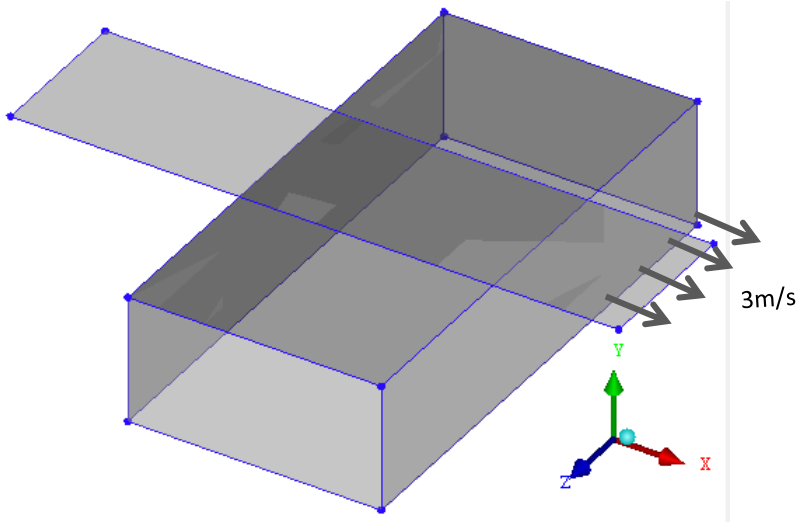

Figure 5- 9: 3D strip-block geometry 2

In the first simulations, the gap between the strip and roll was set at 5mm and 1mm in order to observe the fluid flow in that region. Then, it was reduced to 0.25mm since it has been concluded in section 5-6 that roll and strip are almost in continuous contact with each other. The velocity profiles are shown for two cases, δ=5mm and 1mm (Figures 5-10 and 5-11).

According to the velocity profiles, it can be clearly seen that in the case of larger gap, flow can penetrate into the channel easily compared to the tighter gap. The vortex directions are different in each case.

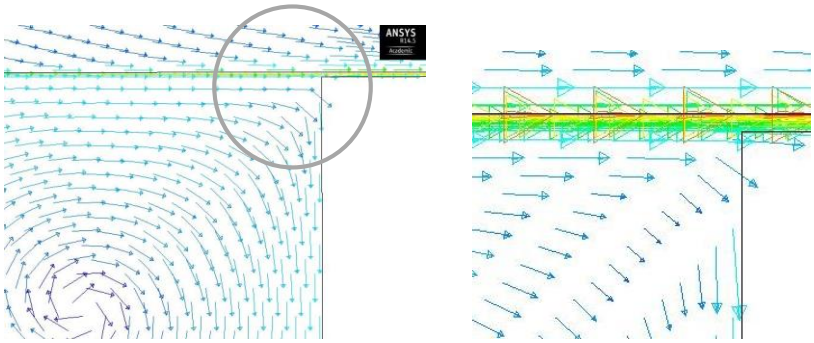

Figure 5- 10: Velocity profile at the entrance of the nip area- δ=1mm

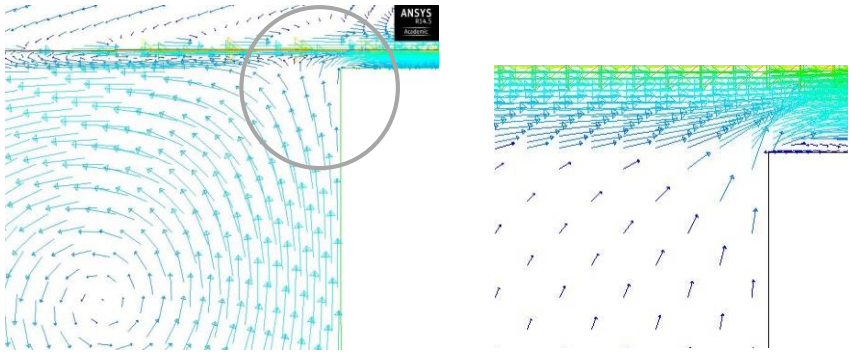

Figure 5- 11: Velocity profile at the entrance of the nip area- δ=5mm

5.9 Strip-Block Studies- Grooved Block

This model is performed to study the effect of the groove geometry on the flow profile at the entrance of a drag flow (Figure 5-12). The straight groove parallel to the moving strip direction resembles the radial pattern groove at the center of the roll. To approximate the effect of different groove pattern on flow profile other than radial, the spiral case is also studied as shown in Figure 5-13.

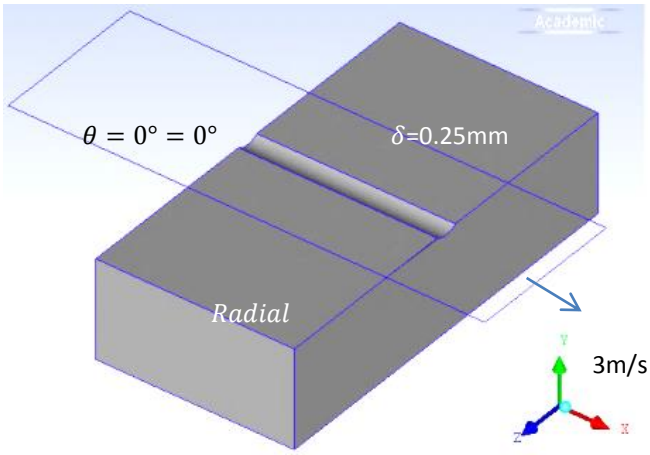

Figure 5- 12: Straight groove in the cavity study- δ=0.25mm

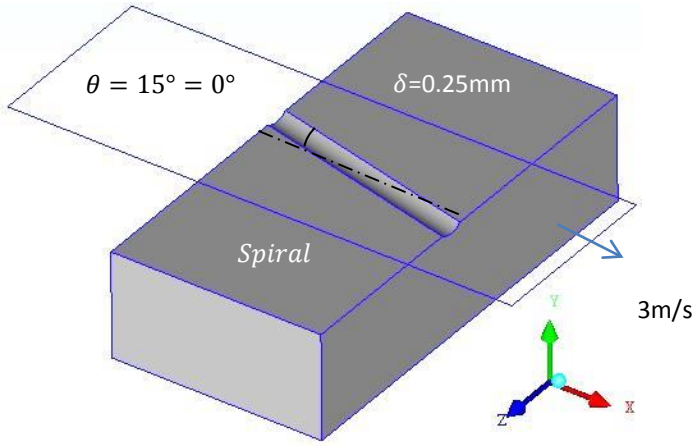

Figure 5- 13: Tilted groove in the cavity study- δ=0.25mm

Different groove angles are then considered on the block. Schematic of these groove angles are shown in Figure 5-14 to 5-15.

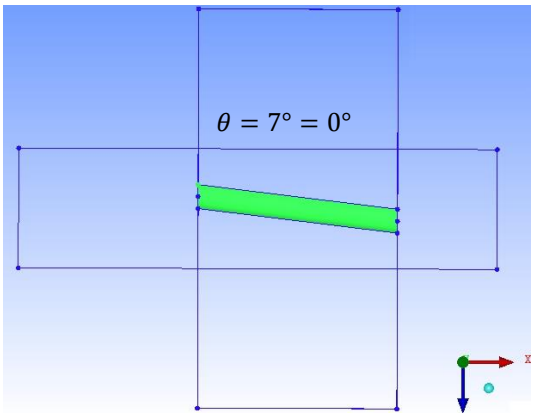

Figure 5- 14: Tilted groove position for θ=7°- Top view

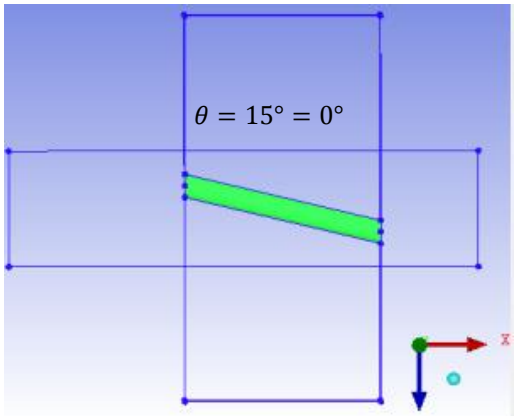

Figure 5- 15: Tilted groove position for θ=15°- Top view

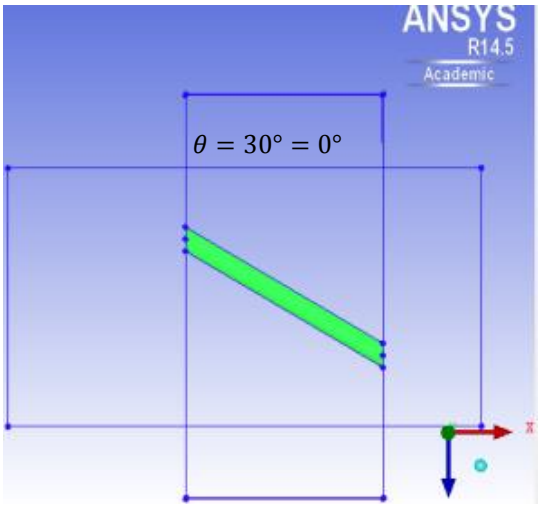

Figure 5- 16: Tilted groove position for θ=30°- Top view

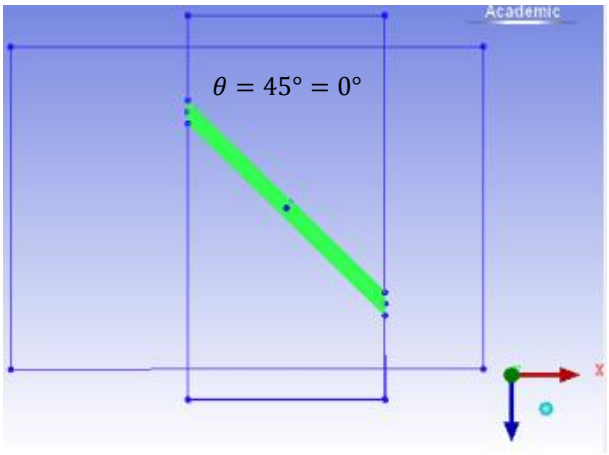

Figure 5- 17: Tilted groove position for θ=45°- Top view

To create a proper mesh grid, mesh resolution has to be fine enough, especially inside the groove and in the gap region. As explained in prior sections, one of the project challenges was creating high resolution grid at the nip region and inside the groove channel. Since the groove geometry 2 is made from intersection of 3 circles (Figure 5-18), the surface elements at both ends of the groove are always skewed with poor quality. To maintain the mesh grid quality at the mentioned area, the groove geometry is modified by deleting the two regions at both groove ends as shown in Figure 5-19.

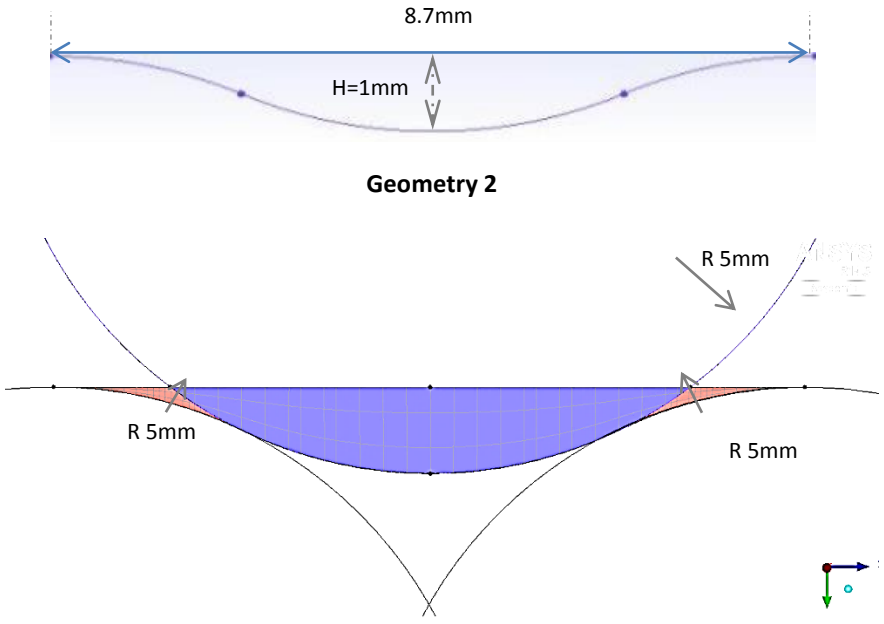

Figure 5- 18: Groove geometry 2- Intersection of 3 circles

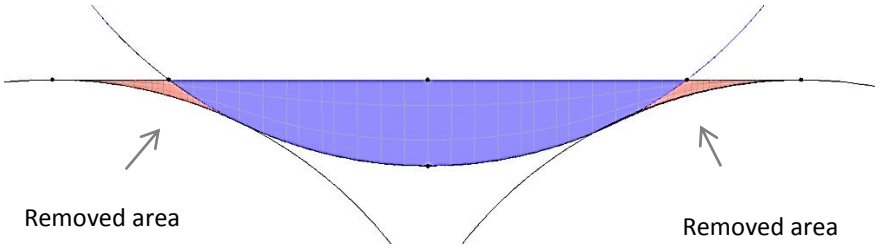

Figure 5- 19: Modified geometry

Simulation is performed using turbulent flow for each case. Velocity profile of each case is shown in the following pictures. The flow profile at the entrance of the nip region is depicted to see any significant phenomenon at the roll center for the straight groove and tilted groove. Pictures on the left show the plane that the velocity profiles are shown onto it and the pictures on the right show the velocity profiles at the nip region entrance for each case. According to the velocity profiles which are shown for each case it can be concluded that the flow at the entrance of the gap appears similar for all of the cases.

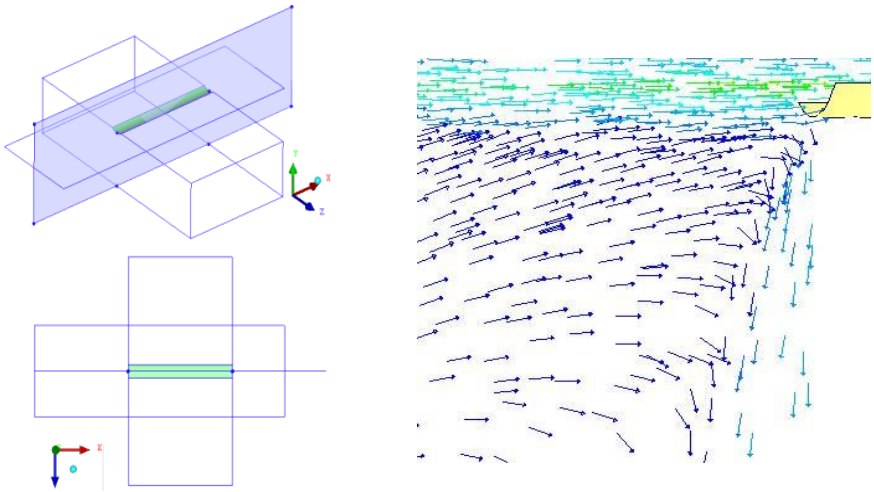

Figure 5- 20: Velocity Profile for groove angle θ=0°

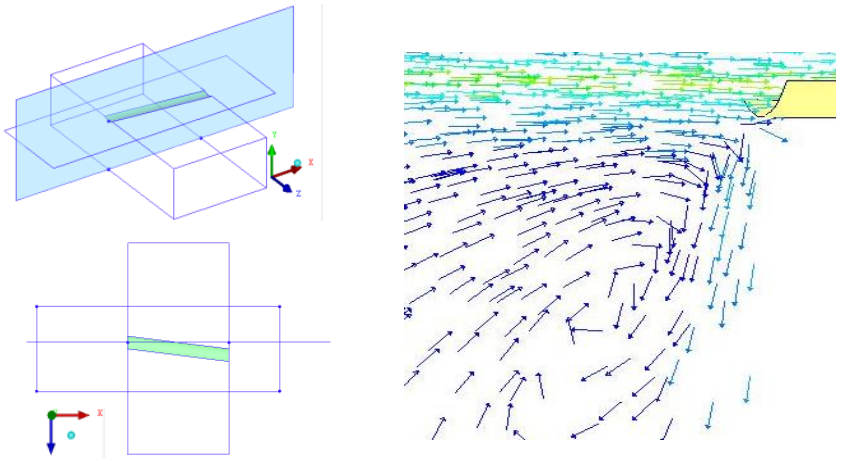

Figure 5- 21: Velocity Profile for groove angle θ=7°

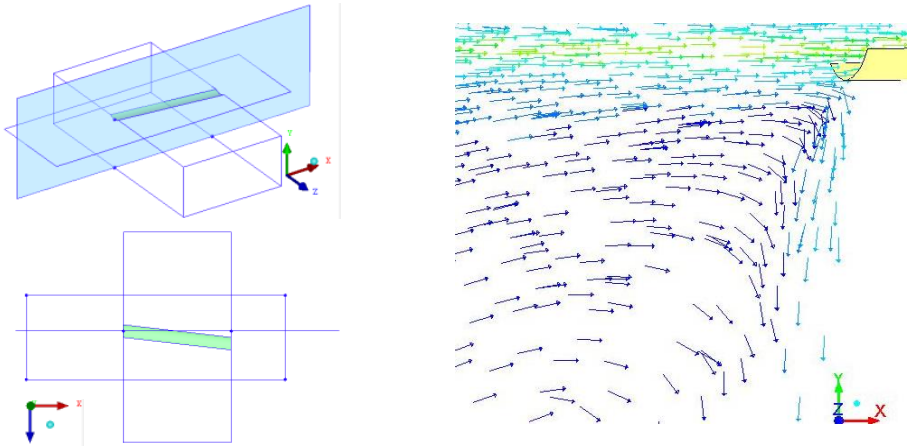

Figure 5- 22: Velocity Profile for groove angle θ=15°

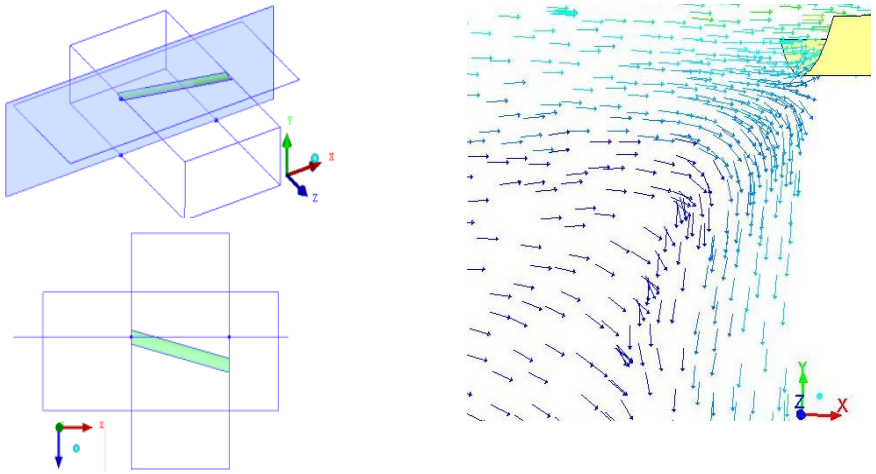

Figure 5- 23: Velocity Profile for groove angle θ=30°

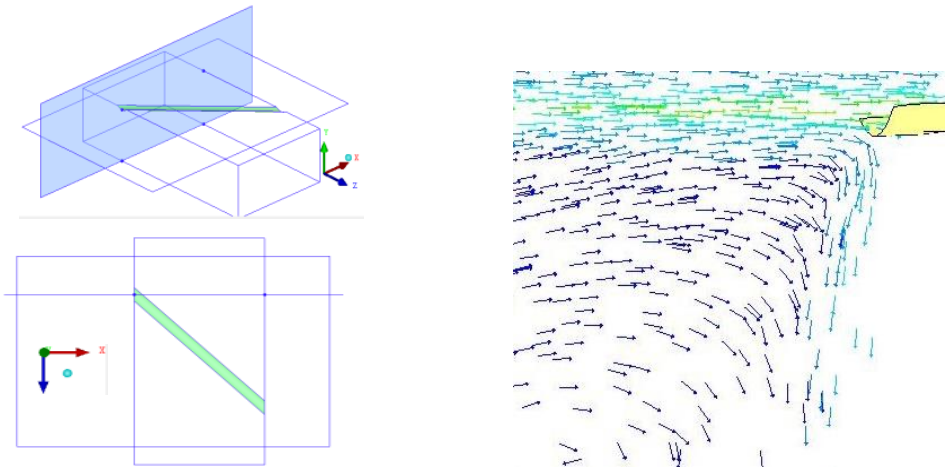

Figure 5- 24: Velocity Profile for groove angle θ=45°

5.10 Conclusions

Building upon the bath modeling results, 2-D modeling of the flow over groove geometries shows that the flow patterns are similar in geometries 1 and 3. In the strip-block study, the velocity profile are depicted at the entrance of the nip region in each tilted groove. It was found that the velocity field at the nip section for different groove angles are similar.

Chapter 6

6 Free Surface Study

Advanced high performance steel requires stability in the coating process. In this chapter, using computational fluid dynamics, the bath liquid-air is modeled at the free surface. The purpose of this work is the study of fluid behaviour at the interface between the liquid and air. Excess zinc falls down to the bath after being picked up by the strip which creates a wave motion on the free surface of the bath. This wave on the bath free surface can pick up the suspended dross particles, which in turn can affect the process stability. Process stability is significant to produce high quality homogeneous coating in a hot- dip galvanizing bath. This study is aimed at modeling the local fluid at the meniscus of the strip and simulating the wave motion at the free surface.

6.1 Air entrainment

Extensive research has been conducted to study the critical velocity at air-entrainment. The critical velocity is the velocity when air entrainment begins. Correlation between the critical velocity, surface tension and viscosity has been well investigated. Equation 6-1 shows this correlation.

$$V_c = k\,(\sigma/\mu)^n \tag{6-1}$$

Where, V_c , σ and μ are the critical velocity at air-entrainment, surface tension (N/m) and is the viscosity (kg/m.s), respectively. Table 6-1 shows the summary of some experimental studies in determining this correlation.

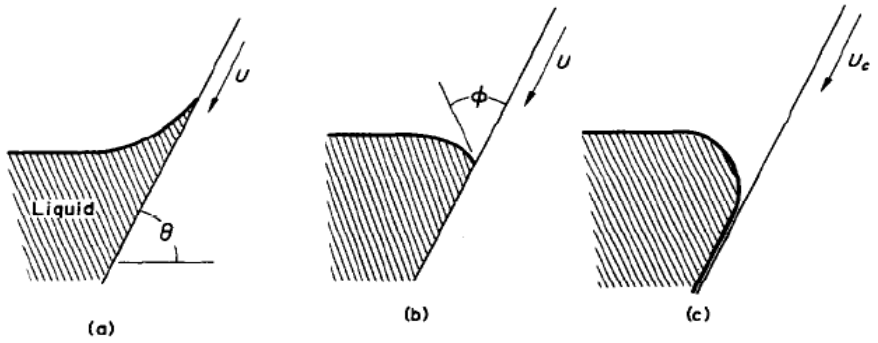

Figure 6- 1: Stages leading to air-entrainment [57]

Table 6- 1: Correlation between critical velocity, surface tension and viscosity

Work by	Type of surface	Regression equation		Regression coefficient (r)
		k	n	
Kennedy [58]	2.5cm wide polyester tapes	1.2	0.71	0.99
Guttof [59]	16.0cm wide gelatine subbed polyester tape	1.51	0.74	0.99
Perry [60]	Magnetic tape	0.95	0.71	0.99
Wilkinson [57]	Pre-wetted rotating drum	1.72	0.91	0.99
Burley [61]	Various tape width and angles of entry	1.14	0.77	0.99

With the known parameters such as surface tension and fluid viscosity: σ(zinc-air@465℃)=0.789N/m and μ=0.004 kg/m.s, the critical velocity is calculated for the galvanizing bath, V_c= 50-100m/s. Hence, it can be concluded that $V_{strip} \ll V_c$ inside the bath due to the strip motion.

6.2 Free-Surface Modeling

To model the fluid motion at the free surface of a galvanizing bath, the Volume of Fluid multiphase model has been used. Ansys FLUENT is employed using realizable k-e turbulent model and accounting the surface tension effects on the free surface.

6.3 VOF Multiphase Model

"Volume of Fluid" multiphase modeling is an Eulerian-Eulerian method of surface-tracking technique which can be used for two or more immiscible fluids. In this approach liquid and gas phases are treated as interpenetrating continua. This model is helpful where the study of interface between two fluids is of interest such as free-surface flows, sloshing and the motion of liquid after a dam break and the prediction of jet breakup.

In this approach, the concept of phasic volume fraction is defined because the volume of a phase cannot be occupied by the other phases. It can be concluded that volume fractions are assumed to be functions of space and time [62].

Continuity and the Navier Stokes equation are solved in the computational domain to conserve mass and momentum. The volume fraction of the fluids in each grid cell is tracked in the domain.

Interface tracking between the liquid and solid phases is conducted by the solution of continuity equation for the volume fraction of one of the phases. The continuity equation for the q^{th} phase is written in equation 6-2 [62].

$$\frac{1}{\rho_q}\left[\frac{\partial}{\partial_t}\left(\varepsilon_q\rho_q\right) + \nabla.\left(\varepsilon_q\rho_q\overrightarrow{v_q}\right) = \sum_{p=1}^{n}(\dot{m}_{pq} - \dot{m}_{qp})\right] \qquad (6\text{-}2)$$

Here, ρ and $\vec{v}$ are density and velocity respectively. p and q are arbitrary phases, $\dot{m}$ is the mass transfer and ε is the volume fraction. When ε equals 1 it means the cell is fully occupied by the liquid and when has no value, it refers to an empty cell for that fluid. The values between 0 and 1 indicate that the cell contains the interface between the q^{th} fluid and one or more other fluids.

In Ansys FLUENT, this equation can be solved in an implicit or explicit scheme. When the implicit scheme is used for time discretization, volume fraction values are calculated at each time step. Whereas in the explicit scheme, volume fraction data are used for the previous time step.

6.4 Surface Tension

The continuum surface force is used for surface tension effect first proposed by Brackbill *et al.* [63]. This model is available in Ansys FLUENT. It implements the addition of surface tension as a source term in the momentum equation.

6.5 Computational Domain

Multiphase Volume of Fluid is used in computational domain consisting of zinc and air. According to the bath geometry displayed in Figure 6-2, a two-dimensional domain is studied. ICEM CFD has been employed to generate the grid mesh. Figure 6-3 and 6-4 demonstrate the mesh resolution near the strip surface and at the liquid interface. The fine mesh has been used in the solver after performing grid independence test.

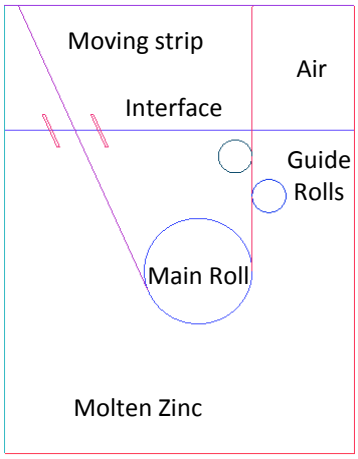

Figure 6- 2: Bath geometry

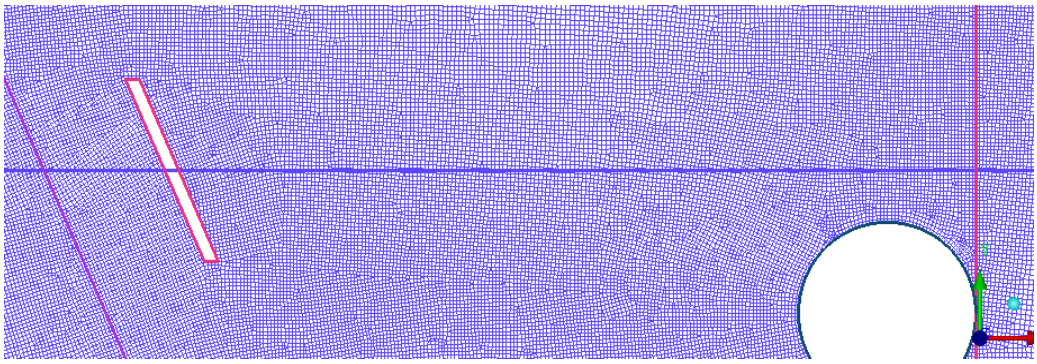

Figure 6- 3: Interface grid display

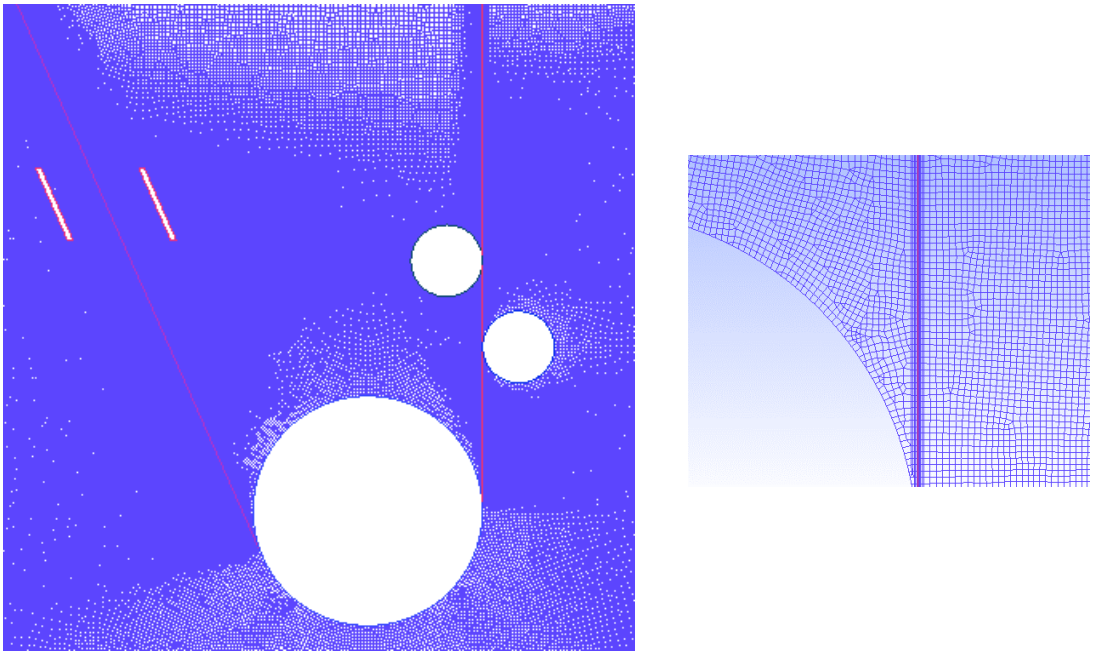

Figure 6- 4: Gird display of the galvanizing bath

6.6 Problem setup and boundary conditions

VOF multiphase model k-ε realizable turbulent model has been used for the fluid and continuous moving wall with constant velocity and no-slip condition for the strip. Simulation has been undertaken in the transient condition using explicit discretization scheme. Molten zinc is considered for the primary phase with density and viscosity of ρ=6600kg/m^3 and μ=0.004kg/m.s. Secondary phase is occupied by air with density and viscosity of ρ=1.225kg/m^3 and μ=1.79e-05kg/m.s, respectively.

Continuum surface force model has been used for the liquid-gas phase interaction. Other boundary conditions have been set according to full bath model: moving strip velocity: 3m/s, main roll rotational velocity 7.5rad/s and guide rolls: 24 rad/s. Left, right and bottom walls are assumed as fixed walls with no-slip conditions, top wall: outflow. Time steps are variable between 0.1-1ms.

6.7 Start-up procedure

In order to validate the VOF model in Ansys FLUENT two well-known cases have been simulated and compared with the literature: plunging tape problem [57-65] and wave generation in a tank with moving oscillatory wall problem [66,67].

In order to start the simulation, a procedure known as pre-wetting or start-up has been performed to prevent any probable jump of the fluid due to the high velocity of the moving objects in the bath. Hence, the velocity of the moving hardware is increased in three phases: from 0-0.03m/s, then from 0.03-0.3 and from 0.3-3m/s which is the actual operating bath condition.

6.8 Results and discussions

Because of the continuous strip motion into the bath and the surface tension between the air and zinc fluid, a curved shape meniscus is generated where the strip leaves the bath. On the other hand, at the strip exit region the outward meniscus is formed. This shape becomes steady when the process is in a steady state condition. Excess zinc then falls back to the

bath by passing over the meniscus surface. Therefore, the fluid film has a wavy shape along the strip.

The phase boundary between air and zinc fluid is shown as colored phase fractions. Here blue and red colors indicate the air and molten zinc, respectively. The spectrum shown in these plots refers to the volume fraction at the interface.

As shown in the calculation for the air- entrainment in section 6-1, it was found that there is no air entering the bath from the strip entry region.

To determine the general fluid flow structure, meniscus formation and to model the fluid fallback and wave motion at the interface, initially the guide rolls and snout are not accounted for the simulation. Separately, simulation is undertaken including the effects of the snout and the guide rolls with the detailed data for the velocity field near the interface of the bath. Figure 6-5 displays an instantaneous volume fraction at a certain time t=0.05s. At this time, the fluid starts to be picked up by the strip leaving the bath. Better views of the fluid structures on the strip are displayed in Figure 6-6 at t=0.29s. They show the formed fluid meniscus where the strip leaves the bath in addition to the curved shape of the fluid at the strip entrance region. Figure 6-7 indicates the motion of the wave at the interface caused by the fallback of excess fluid on the strip at t=0.59s. Figure 6-8 depicts the zoom-in of the fluid at the meniscus at t=2.78s.

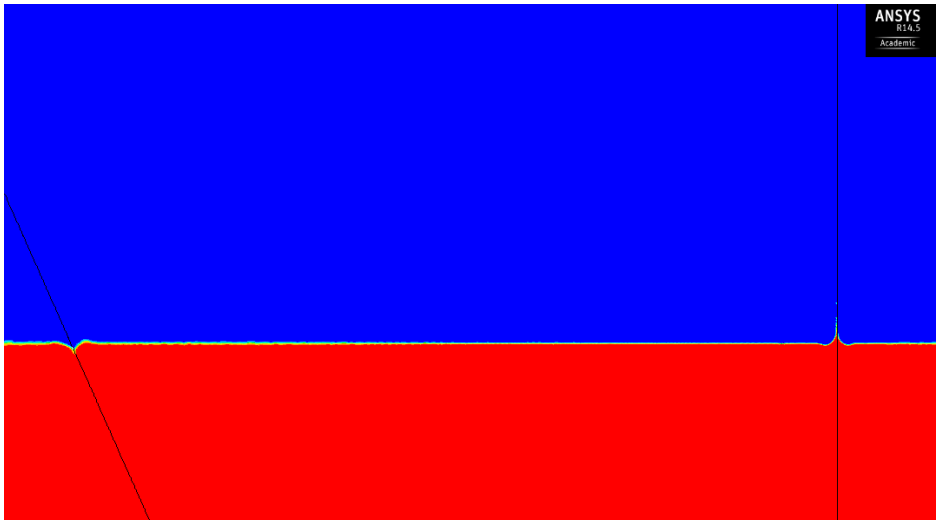

Figure 6- 5: Volume fraction in the bath at t=0.05s

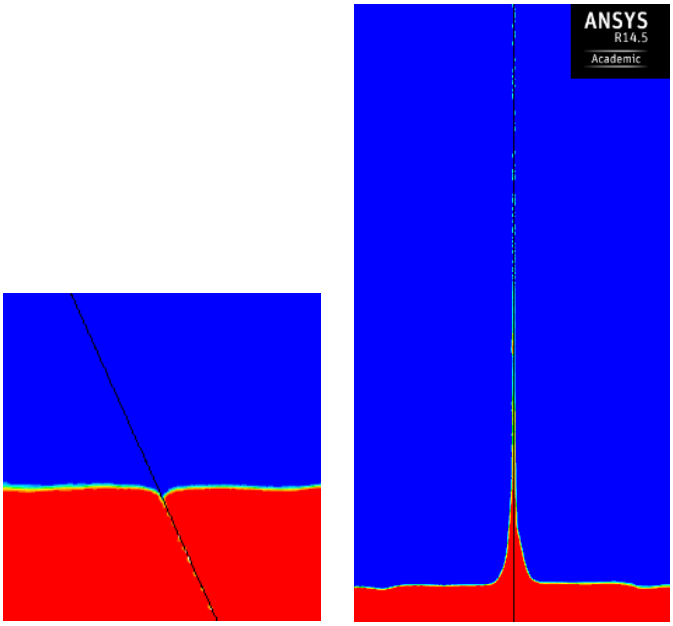

Figure 6- 6: Volume fraction at the bath at t=0.29s

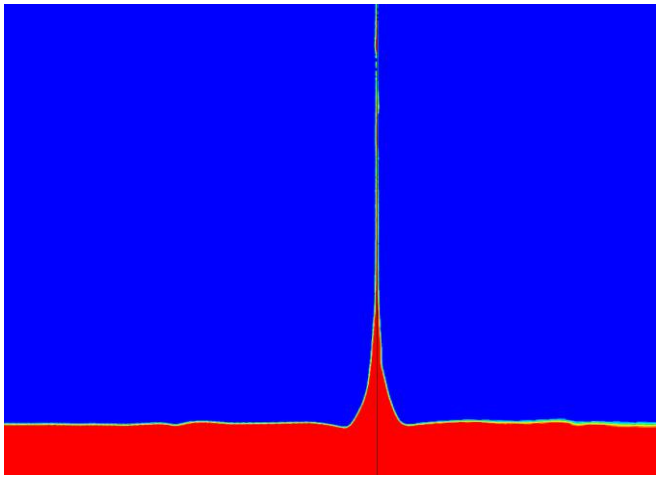

Figure 6- 7: Volume fraction at the bath at t=0.59s

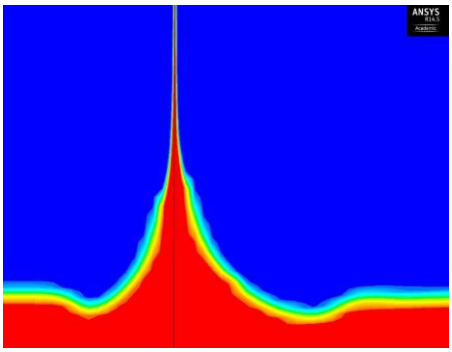

Figure 6- 8: Fluid behaviour at the meniscus at t=2.78s

The thickness of the fluid film on the strip becomes more stable after being dragged by the strip. A coarse approximation of coating thickness of fluid film is measured (t=500μm) as shown in Figure 6-9.

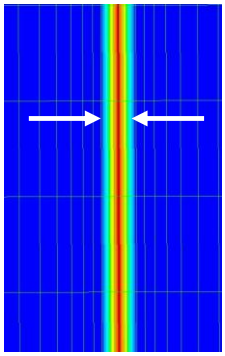

Figure 6- 9: Coating layer formed on the strip

The following figures show the velocity vectors in the computational domain for the fluid and gas phase. Fluid vectors with fixed and various lengths are displayed to indicate the direction of the flow. The mesh density was increased near the interface and near the strip in order to capture the fluid flow at the interface and the film motion near the meniscus. Figure 6-10 displays the velocity vectors for the bath fluid where the strip exits the bath. It should be noted that for better understanding of the direction of the velocity vectors, these vectors are plotted with constant size.

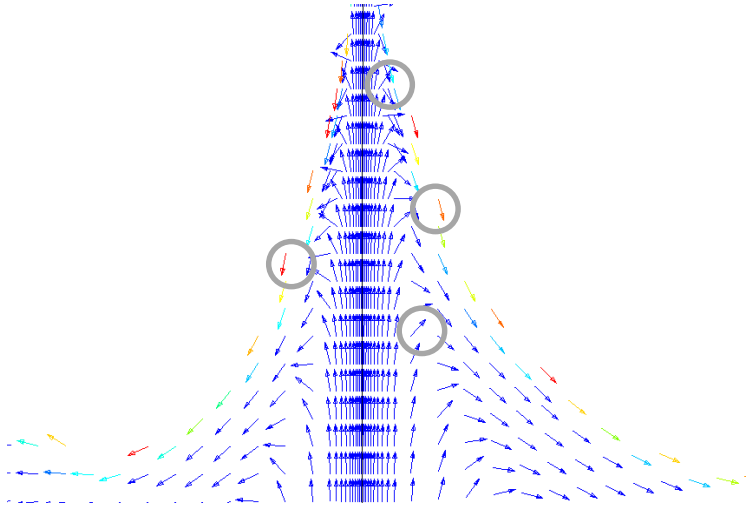

Figure 6- 10: Liquid velocity vectors on the strip where it leaves the bath

The liquid flow is depicted separately in Figure 6-11 to show the influence of the wave motion along the interface. Fluid flow pattern is depicted for the liquid phase near the interface at the top of the roll. This is the area of interest as shown in 6-2 and 6-3.

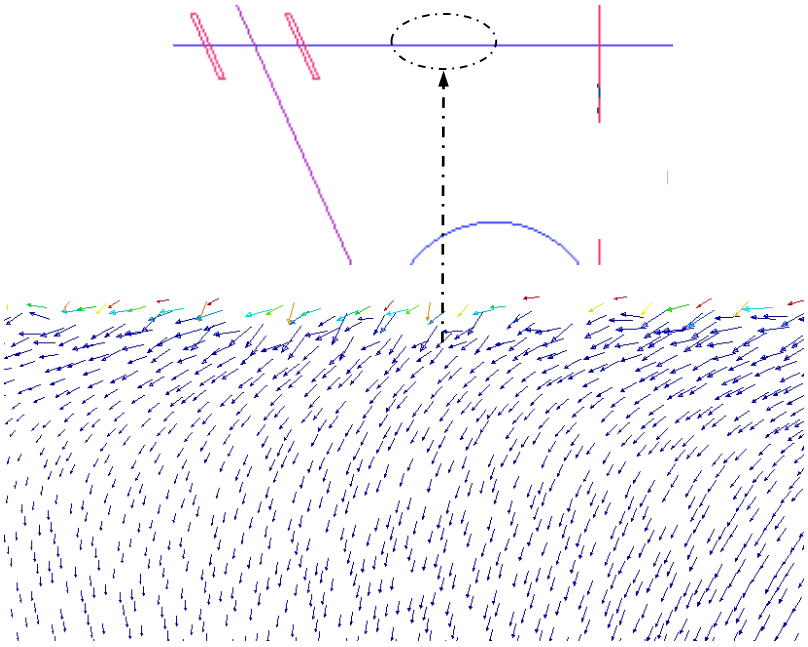

Figure 6- 11: Liquid velocity vectors for the fluid on top of the roll between the strip entry and exit region

According to the observations from industry, the wave motion on the interface tends to pick-up the top dross particles and creates coating problems for the strip which is submerging to the bath at the entry region. Therefore, it is significant to study the effect of the snout and guide rolls in terms of the wave created on the interface. Simulation has been carried out for the case including guide rolls and the snout. Velocity vectors within the bath on top of the roll are shown in Figure 6-12 for the liquid phase. Better views for the velocity field in the bath are shown through Figure 6-13-6-14. Based on the results, it can be seen that in the presence of the guide rolls and snout, the fluid direction below the interface is different from the results have been achieved from the case without considering the guide

rolls. The larger velocity vectors at the interface are due to the wave motion at the free surface and transient effect of the problem.

It was shown that the guide roll on the left side of the strip which is closer to the free surface, has more influence on the interface. The vortex, which resulted from the motion of the left guide roll, can create a flow in direction toward the strip. This flow is in the opposite direction with the wave motion from the excess fluid on the strip.

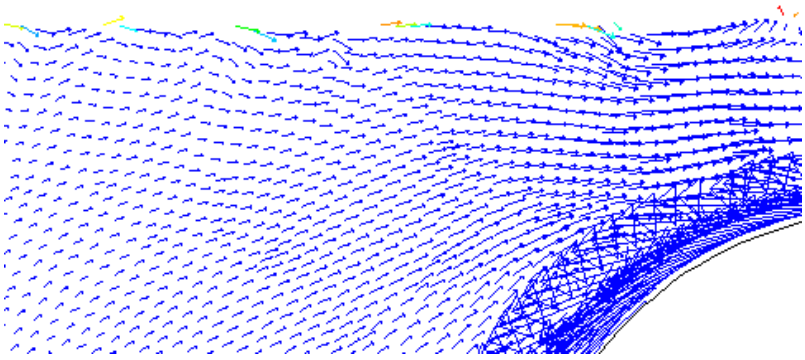

Figure 6- 12: Velocity vectors for the liquid- close to the guide roll

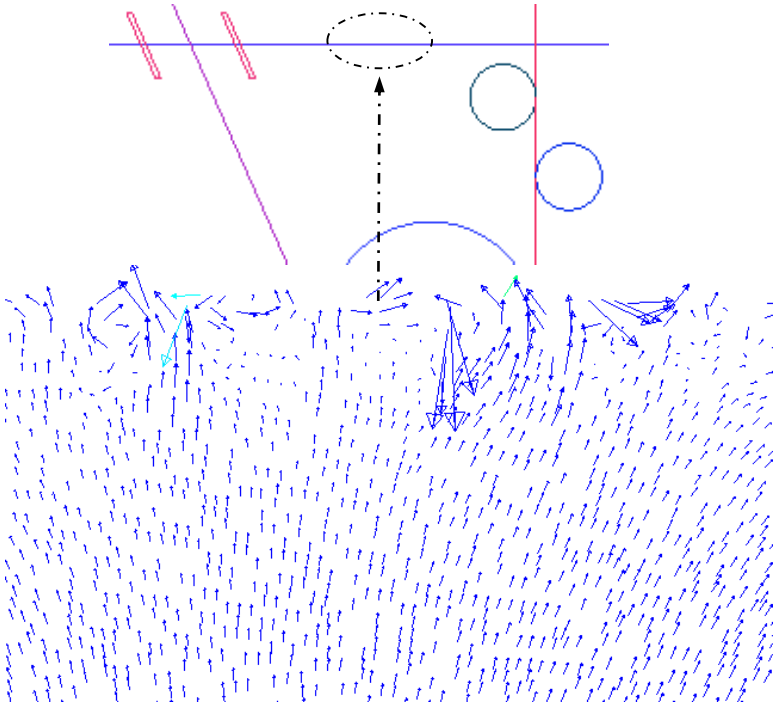

Figure 6- 13: Liquid velocity vectors for the fluid on top of the roll between the strip entry and exit region

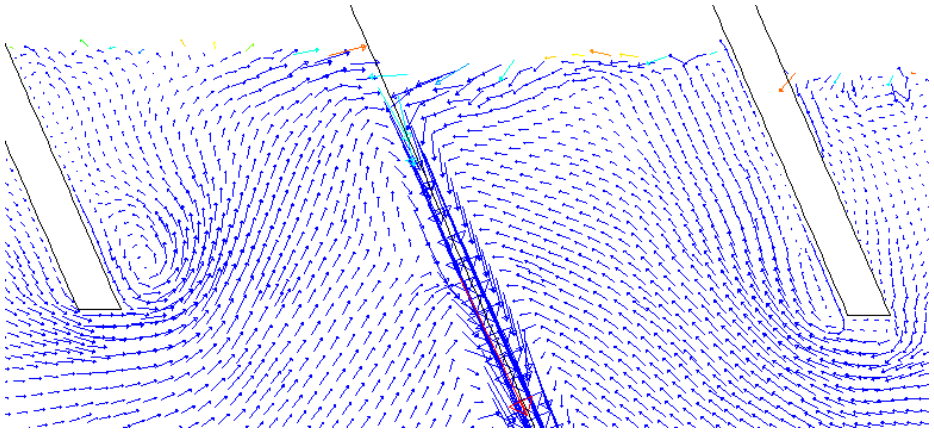

Figure 6- 14: Velocity vectors for the liquid at the snout region

6.9 Conclusions

A study has been conducted to understand whether there is probable air-entrainment in the bath due to the high velocity of the strip into the bath. Calculations showed there is no air entrainment due to the high surface tension and low viscosity of the zinc fluid.

The fluid flow at the free surface of galvanizing bath is modeled using Ansys FLUENT software in two dimensions. VOF multiphase model flow is used with k-e model and applying the defined boundary conditions.

It is concluded that the simulation results are qualitatively in accordance with the observations from the industry. Based on the results, the meniscus is formed once the process became steady. Coating layer on the strip is formed after resolving the mesh grid at the moving strip and at the interface. This model was able to predict the fluid film thickness on the strip.

This process was accomplished by the pre-wetting process in the domain which let the fluid flow be stable in the bath. It was observed that due to the fallback from the excessive coating on the strip, a short wave motion is created which moves toward the strip entry region. The velocity vectors are shown at this region for each phase. In order to study the effect of the snout and guide rolls on the created wave at the interface, simulation has been carried out with and without presence of guide rolls and snout. It was observed that in the case that the guide rolls and snout exist, the vortex resulted from the rotation of the left

guide roll creates a fluid flow in direction toward the strip and in the opposite direction of the wave motion. Snout can deviate the interaction of the top dross particle with the strip at the entry region. Therefore, it can be concluded that the presence of the guide rolls and snout can mitigate the wave motion is going toward the strip entrance area. This is significant because based on the reports from industry this wave motion on the interface can pick-up the top dross particles and create coating problems for the strip at the entry region.

It should be noted that for the simplicity, this simulation has been performed in two dimensions. Hence, the actual three dimensions flow is not studied. Also, in this study, the effect of wiping gas jet on the excessive coating on the strip was not accounted for.

Chapter 7

7 Summary

Based on the extensive literature review it was concluded that previous studies have been focused on the bulk turbulent flow pattern in the galvanizing bath, analysis of the effect of operating parameters on the flow field, dross concentration in the "V-section" and dross particle size and chemistry in the bath.

In summary, this new study is focused on analysing the fluid flow behaviour at the extreme vicinity of the roll where it meets the strip and studying the particle-surface interaction within the bath, as an important key in understanding the dross build-up on the roll surface.

The detailed information about fluid flow in the galvanizing bath has been analysed using CFD modeling. Based on the 3-D fluid flow studies in the bath, it was concluded that the fluid flow in the bath becomes concentrated near the sink roll, where it meets the strip. This is significant because it addresses the dross particle interaction locations on the roll, where the particles most likely agglomerate on the roll surface.

Studying the dynamic behavior of multiphase (liquid–solid) flows was found to be crucial due to its relevance to agglomeration processes in hot dip-galvanizing process. The 3-D liquid- solid flow inside the bath was simulated using different multiphase fluid models. As expected, most of the injected dross particles are observed to become trapped inside the vortices in the center of V-section. The circulating motion of flow in this region drags these bottom dross particles toward the top surface of the sink roll. Findings revealed that the particle fate in the bath strongly depends on its location at the V-section region. Simulation results show that the particles far from the strip edge (near the vicinity of the roll centre) will remain in the V-section and move toward the sink roll top surface. However, particles which are moving from the strip entrance region, near the steel strip edge, are pushed out toward the roll ends. Resulting in collisions of particles with the roll surface. According to the reports from the industry on the location where dross particles agglomerate on the roll, it can be concluded that the observed locations of particle-surface interaction and particle agglomeration are consistent with observations in industry.

A 2-D modeling of the flow over some groove geometries has been undertaken. Based on the results it was concluded that the flow patterns in the second studied groove might be more efficient in terms of providing escape channels for the multiphase flow near the strip-edge region.

The fluid flow at the free surface of galvanizing bath in two dimensions is modeled using Volume of Fluid multiphase approach. It was concluded that the presence of the guide rolls and snout can alter the wave motion toward the strip entrance area. This is significant because based on the reports from industry this wave motion on the interface can pick-up the top dross particles and create coating problems for the strip at the entry region.

References

[1] "55% Aluminum-Zinc Alloy-Coated Steel Sheet" GalvaInfo, 2011 [Online]. Available: http://www.galvinfo.com/ginotes/GalvInfoNote_1_4.pdf

[2] Shim, D., Lee, M., "New CGL of POSCO-Mexico", Asia Pacific Galvanizing Conference, October 2009.

[3] Varadarajan, A., "Dross Formation Mechanism and Development of Wear Resistant Scraper in 55Al-1.5Si-Zn Coating Bath", PhD Dissertation, West Virginia University", 2008.

[4] Nakano, J., Purdy, G.R., Malakhov, D.V., "Modeling of Intermetallic Formation in Hot-dip Galvanizing", XXXI CALPHAD Meeting Proceedings, 2002.

[5] Liu Y.H., Tang N.Y., Zhang L., Denner S.G., Goodwin F., "Dross Formation and Control during Transition from Galvannealing to Galvanizing", 44th MWSP Conference Proceedings, Iron & Steel Society, 781–790, 2002.

[6] Shawki, S. and Abdel Hamid, Z., "Effect of Aluminium Content on the Coating Structure and Dross Formation in the Hot-dip Galvanizing Process", Surface and Interface Analysis, 35: 943–947, 2003.Dunbar, F.C., "Galvanizers Committee Meeting", Canton, OH, 1988.

[7] Kim, Y.W., Kung, S.C., Sievert, W.C. and Patil, R: in Proc., Galvatech89, 120, 1989.

[8] Tang, N.Y., in Proceeding, "Zinc-Based Steel Coating Systems: Production and Performance", TMS Conference, St. Antonio, Texas, TMS, PA, 3-12, 1998.

[9] Ajersch, F., Ilinca, F., Hétu, J.F. and Goodwin, F., "Numerical Simulation of Flow, Temperature and Composition Variations in a Galvanizing Bath", Canadian Metallurgical Quarterly, Vol 44, No 3 pp 369-378, 2005 .

[10] Giorgi, M.L., Guillot, J.B., and Nicolle, R., "Modeling of the Kinetics of Galvanizing Reactions", PR 308-068- Galvatech Conference Proceedings, 2004.

[11] Gagné, M., Paré, A., and Ajersch, F., "Water Modeling of a Continuous Galvanizing Bath" 84th Galvanizers Association Meeting Proceedings, 147-163, Oct. 1992.

[12] Kurobe, J. and Iguchi, M., "Cold Model Experiment on Dynamic Behaviour of Dross in Hot dip Plating Bath", Science and Technology of Advanced Materials, Volume 1 Number 4, 2000.

[13] Shin, D.S., Choi, J. and Lee, S.J., "Velocity Field Measurements of Flow inside Snout of Continuous Hot-Dip Galvanizing Process Using a Single-frame PIV Technique", ISIJ International, Vol. 40, No. 5, 484–490, 2000.

[14] Ouellet, L., Ajersch, F., Ilinca, F., "Numerical Simulation and Validation of Flow in a Galvanizing Bath Using a Water Model," Galvatech'04 Proceedings, 917- 926, 2004.

[15] Toussaint, P., Vernin, P., Symoens, B., Segers, L., Tolley, M., Winand R. and. Dubois, M., "Experimental-Determination of Velocity Flow-Fields In Continuous Hot-Dip Galvanizing Baths", Ironmaking Steelmaking, Vol. 23, 357, 1996.

[16] Ajersch, F., Ilinca, F. and Hétu, J.F., "Simulation of the Flow in a Continuous Galvanizing Bath: Part I. Thermal Effects of Ingot Addition," Metallurgical and Materials Transactions B, 161-170, 2004.

[17] Willis, D. J., Ilinca F., and Ajersch, F., "Fluid Flow Modeling in a 55% Al-Zn Pot" Galvatech'04, 6th International Conference on Zinc and Zinc Alloy Coated Steel, AIST, Warrendale, PA, 905, 2004.

[18] Willis, D.J., Ilinca, F., Ajersch, F. and Setargew, N., "Fluid Flow Modelling in a 55% Al-Zn Coating Metal Pot", Progress in Computational Fluid Dynamics, 7(2-4), 183-194, 2007.

[19] Pare, A., Binet, C., and Ajersch, F, "Numerical Simulation of 3-Dimensional Flow in a Continuous Strip Galvanizing Bath", Galvatech 95, 695-706, 1995.

[20] Paik, D.J., Hong, M.H., Huh, Y., Park, J.H., Chae, H.K., Park, S.H., and Choun, S.Y., "Metastable Phases of Dross Particles Formed in a Molten Zinc Bath and Prediction of Soluble Aluminium During Galvannealing Processes", The Minerals, Metals & Materials Society and ASM International, 2012.

[21] Tang, N.Y., Dubois, M., Goodwin, F.E., "Progress in Development of Galvanizing Bath Management Tools" Proc. Galvatech'98, Chiba, Japan, 76-83, 1998.

[22] Chen, X. and Wang, J., "A Comparison Of Two-Fluid Model, Dense Discrete Particle Model and CFD-DEM Method For Modeling Impinging Gas–Solid Flows", Powder Technology 254 94–102, 2014.

[23] Hryba, D., Cardozoa, M., Ferroa S. and. Goldschmit, M., "Particle Transport in Turbulent Flow Using Both Lagrangian and an Eulerian Formulation", International Communications in Heat and Mass Transfer, 2009.

[24] Kloss, C., Goniva, C., Aichinger, G. and Pirker, S., "Comprehensive DEM-DPM-CFD Simulations Model Synthesis, Experimental Validation and Scalability", 7th Int. Conference on CFD in the Minerals and Process Industries CSIRO, Melbourne, Australia, Dec. 2009.

[25] Pope, S. B.: Turbulent Flows, Cambridge University Press, 2000.

[26] Jones, W.P. and Launder, B.E., "The Calculation of Low Reynolds Number Phenomena with a Two-Equation Model of Turbulence", Int. J. Mass Heat Transfer. Vol. 16, 1119-1130, 1973.

[27] Abuzeid, S., Busnaina, A.A. and Ahmadi, G., "Wall Deposition of Aerosol Particles in a Turbulent Channel Flow", J. Aerosol Sci., Vol. 22, No. 1, 43-62, 1991.

[28] Hryba, D., Cardozoa, M., Ferroa S. and. Goldschmit, M., "Particle Transport in Turbulent Flow Using Both Lagrangian and an Eulerian Formulation", International Communications in Heat and Mass Transfer, 2009.

[29] Elimelech, M., Jia, X., Gregory, J., Williams, R., "Particle Deposition & Aggregation: Measurement, Modelling and Simulation", Butterworth-Heinemann Ltd., Aug, 1998.

[30] Guha, A., "Transport and Deposition of Particles in Turbulent and Laminar Flow", Annul Review, Fluid Mech. 40:311-341, 2008.

[31] Ounis, H. and Ahmadi, G., "A Comparison of Brownian and Turbulent Diffusions", Aerosol Science Technology, Vol. 13, 47-53, 1990.

[32] Wood, N. B., "A Simple Method for the Calculation of Turbulent Deposition to Smooth and Rough Surfaces", Journal of Aerosol Science. Vol. 12. No 3. 27-290, 1981.

[33] Zaichik, L., Vladimir M., Alipchenkov, Emmanuil G. and Sinaiski, "Particles in Turbulent Flows", John Wiley & Sons, 2008.

[34] Caporaloni, M., Tampieri, F. Trombetti, F. and Vittori, O., "Transfer of Particles in Nonisotropic Air Turbulence", Jouranl of Atmos. Science., 32, 565–568, 1975.

[35] White, F. M.: Ouellet's [7] numerical study, which was validated by PIV experimental method discussed in chapter 3, also conforms to the obtained simulations results from the 3-D bath model in the vortex formed on top of the sink roll at the center line of the galvanizing bath.

[36] Ansys FLUENT, Release 14.5 User manual, Multiphase Flow.

[37] Salim, S.M. and Cheah, S.C., "Wall y+ Strategy for Dealing with Wall-bounded Turbulent Flows", Proceedings of the International Multi Conference of Engineers and Computer Scientists, Vol. II, IMECS 2009, Hong Kong (2009).

[38] Liu, Y.H., Tang N.Y., Zhang L., Denner S.G., Goodwin F., "Dross Formation and Control During Transition from Galvannealing to Galvanizing", 44th MWSP Conference Proceedings, Iron & Steel Society, 781–790 (2002)

[39] Karimi, S., Mansourpour, Z., Mostoufi N. & Sotudeh-G., R., "CFD-DEM Study of Temperature and Concentration Distribution in a Polyethylene Fluidized Bed Reactor, Particulate Science and Technology", an International Journal, 29:2, 163-178, 2011.

[40] Sapp, E. G., Hickman, M. D., Brooks, S. E., and Piper, J. M. "Method, System and Apparatus for Scraping a Roll Surface in a Molten Metal Coating Process", 2009.

[41] Kurobe, J. and Iguchi, M., "Cold Model Experiment on Dynamic Behaviour of Dross in Hot dip Plating Bath", Science and Technology of Advanced Materials, Volume 1 Number 4, 2000.

[42] Ibsen, C.H., Helland, E., Hjertager, B.H., Solberg, T., Tadrist, L., Occelli, R., "Comparison of multi-fluid and discrete particle modelling in numerical predictions of gas particle flow in circulating fluidised beds", Powder Technology 149, 2004.

[43] Chu, K.W. , Wang, B., Yu, A.B., Vince, A., Barnett, G.D., Barnett, P.J., "CFD–DEM study of the effect of particle density distribution on the multiphase flow and performance of dense medium cyclone", Minerals Engineering 22 893–909, 2009.

[44] Rosato, A., Prinz, F., Standburg, K.J., Swendsen, R., "Monte-Carlo, simulation of particulate matter segregation", Powder Technology 49, 59–69, 1986.

[45] Xizhong, C. and Wang, J.,"A Comparison Of Two-Fluid Model, Dense Discrete Particle Model and CFD-DEM Method For Modeling Impinging Gas–Solid Flows", Powder Technology 254 94–102, 2014.

[46] Feng, Y. Q., Xu, B. H., Zhang, S. J. and Yu, A. B., "Discrete Particle Simulation of Gas Fluidization of Particle Mixtures", AIChE Journal, Particle Technology and Fluidization, Vol. 50, No. 8, August 2004.

[47] Kloss, C., Goniva, C., Aichinger, G., and Pirker, S., "Comprehensive DEM-DPM-CFD Simulations Model Synthesis, Experimental Validation and Scalability", 7th International Conference on CFD in the Minerals and Process Industries CSIRO, Melbourne, Australia, 2009.

[48] Cundall, P. A. and Strack, O. D. L., "A Discrete Numerical Model For Granular", Assemblies. Géotechnique, 29(1), 47–65, 1979.

[49] Apostolou, K., Hrymak, A.N., "Discrete element simulation of liquid-particle flows", Computers and Chemical Engineering 32 (2008) 841–856, March 2007.

[50] Kloss, C., Pirker, S., Presentation on "Coupling of DEM and CFD simulation and experiment", Christian-Doppler Laboratory on Particulate Flow Modelling, March 2009.

[51] Di Renzo, A. and Maio, F. P. Di, "Comparison of contact-force models for the simulation of collisions in DEM-based granular flow codes", Chemical Engineering Science, 59, 525-541, 2004.

[52] Tsuji, Y., Tanaka, T. and Ishida, T., "Lagrangian numerical simulation of plug flow of cohesionless particles in a horizontal pipe", Powder Technology, , vol. 71, 239, 1992.

[53] Ong, G.P., Fwa, T.F. & ASCE, M., "Transverse Pavement Grooving against Hydroplaning. I : Simulation Model", pp.441–449, June 2006.

[54] Kim, T. W., H.-Y., J., ”Hydroplaning Simulations for Tires Using FEM, FVM and an Asymptotic Method”, International Journal of Automotive Technology, 11(6), 901-908, 2010.

[55] Gallaway, B. M., Ivey, D. L., Hayes, g. G., Ledbetter, W. G., Olson, R. M., Woods, D. L. and Schiller, R. E., “Pavement and Geometric Design Criteria for Minimizing Hydroplaning”, Federal Highway Administration Report, No. FHWA-RD-79-31, Texas Transportation Institute, Texas A&M University, USA, 1979.

[56] Kumar, S. ”Analyzing Effect of Tire Groove Patterns on Hydroplaning Speed, Journal of the Eastern Asia Society for Transportation Studies”, 2009.

[57] Wilkinson, W.L., “Entrainment of air by a solid surface entering a liquid/air interface”, Chemical Engineering Science, 30 1227, 1975.

[58] Burley, R. and Kennedy, B. S., “A Study of the Dynamic Wetting Behaviour of Polyester Tapes”, The British Polymer Journal, 8 140,1976.

[59] Gutoff, E. B. and Kendrick, C. E., Dynamic Contact Angles, AIChE Journal 28(3), 459-466, 1982.

[60] Perry, R. T., Ph.D. Dissertation, ““Fluid Mechanics of Entrainment through Liquid-Liquid and Liquid-Solid Junctures”, University of Minnesota, U.S.A. 1967.

[61] Burley, R., Jolly, R.P.S., “Entrainment of air into liquids by a high speed continuous solid surface”, Chemical Engineering Science, 39, 1357,1984.

[62] Ansys FLUENT manual, Version 14.5, Multiphase flow modeling Chapter.

[63] Brackbill, J. U., Kothe D. B., and Zemach C., “A Continuum Method for Modeling Surface Tension”, Journal of Computational Physics, 100. 335–354. 1992.

[64] Cohu, O. and Benkreira, H., “Air entrainment in angled dip coating”, Chemical Engineering Science, Vol. 53, No. 3, 553-540, 1998.

[65] Buonopane, R. A., Gutoff, E. B., and Rimore M. M. T., Effect of Plunging Tape Surface Properties on Air Entrainment Velocity, AIChE Journal, 32(4): 682-68306, June 2004.

[66] Ansys FLUENT tutorial, Tutorial 10.0, “Simulation of Wave Generation in a Tank”, Ansys Fluent Inc. August 18, 2005.

[67] Peng, J., Liu Y., Liu, J. and Li, Y., “Research of Numerical Wave Generation and Wave Absorption, Simulation Based on Momentum Source Method”, International Journal of Digital Content Technology and its Applications, Volume7, No.1, Jan. 2013.

Appendix A

The purpose of this study is to determine the groove geometry parameters which affect the hydroplaning. Hydroplaning functionality with respect to the groove geometry was found to be useful to approximate the roll-strip model. Both tire-road model and roll-strip model contain two moving surface flow. The former contains air-water and the latter contains particle-molten zinc. The effects of a groove geometry (depth, width and spacing) and pattern (radial/spiral V.S longitudinal and transverse) on the fluid flow at the contact region are studied.

Hydroplaning

Hydroplaning is a major safety concern, which occurs when a layer of water prevents direct contact of tire and road. The main cause of hydroplaning is loss of traction and contact force between the tire and wet road. Hydroplaning commences when the vehicle speed becomes high enough that the hydrodynamic pressure of the water between its tires and the road rises and equals the tire inflation pressure [1,2]. Increased hydroplaning velocity means longer contact of tire and wet road.

Hydroplaning phenomenon has been studied numerically and experimentally to understand the effect of groove geometry on tire skid resistance in the past decades. Width refers to the opening distance of the groove in the horizontal coordinate, depth refers to the maximum distance of the groove in vertical coordinate and spacing refers to the distance between centers of two grooves. According to previous studies by Horne *et. al.* [3,4], tire grooves can help in expulsion of water from the tire-road contact region by providing escape channels, thus reducing the hydroplaning risk. Different groove patterns are found to have different influence on hydroplaning velocity. Maycock [5] and Gengenbach [6] have performed extensive experimental studies to understand the hydroplaning velocity as a function of width, depth and groove spacing. They all show that tire groove geometry has a tremendous effect on tire skid resistance. The results show that the groove width is the most effective parameters compared to depth and spacing. It was found that the tire groove width has 23.7% effect in hydroplaning velocity increase. Groove spacing and groove depth parameters showed 20.1% and 5.8% increase, respectively.

In this study, hydroplaning phenomena for a tire with suitable groove geometry can take place at a higher speed and in a longer time due to the lower hydrodynamic uplift force. A summary of the hydroplaning studies is displayed in Table A-1.

Table A- 1: Summary of previous studies on hydroplaning

	Authors	Article Name/Main Learning
1	Kim, T.W. and Jeong, H.Y.	Hydroplaning Simulations for Tires using FEM, FVM and an asymptotic method, International Journal of Automotive Technology, Vol. 11, No.6, pp. 901−908 ,2010
		Hydroplaning velocity and Lift force are studied for two tread patterns
2	Okano, T. and Koishi, M	Hydroplaning Simulation using MSC. Dytran., THE YOKOHAMA RUBBER CO., LTD, 2-1 Oiwake Hiratsuka Kanagawa 254-8601, Japan
		Hydroplaning Velocity for wider groove is the highest (MSC DYTRAN) results were verified by experimental studies
3	Ong., G. P., Fwa, T. F. and ASCE,M.	Transverse Pavement Grooving against Hydroplaning., I: Simulation Model, Journal of Transportation Engineering ASCE, June 2006
		Hydroplaning on transverse groove pavement surface studied. The deeper and wider grooves are found to be more effective
4	Kumar S.S, Anupam, K, Scarpas, T., Kasbergen,C	Study of Hydroplaning Risk on Rolling and Sliding Passenger Car, 5th International Congress, Sustainability of Road Infrastructures, 2012
		Hydroplaning simulation for a rolling and sliding tire for a range of water depth condition. Simulation validation with experimental data
5	Kumar,S.S., Anupam, K and T. F. FWA	Analyzing Effect of Tire Groove Patterns on Hydroplaning Speed, Journal of the Eastern Asia Society for Transportation Studies, Vol.8, 2009
		Effect of Tire Longitudinal, transverse and block treads Groove Patterns on Hydroplaning Velocity. The tires with wider, deeper with less spacing were more effective

Tire Grooving Effect on Hydroplaning

Okano *et al*. [7] studied the tire longitudinal groove effect on hydroplaning. As: A smooth tire, a tire with 9mm longitudinal groove width and one with 18mm as shown in Figure A-1. Figure A-2 shows the flow behaviour around tire contact area and also water jet extrusion from longitudinal groove. Comparing the fluid simulation results for the three tires with

different groove width, it can be clearly seen that the tire with wider grooves (18mm), can provide higher fluid velocity (in the same direction of the fluid flow) than the tire with 9mm groove width and the smooth tire. The comparison of the experimental results with the simulation results is depicted in Figure A-3.

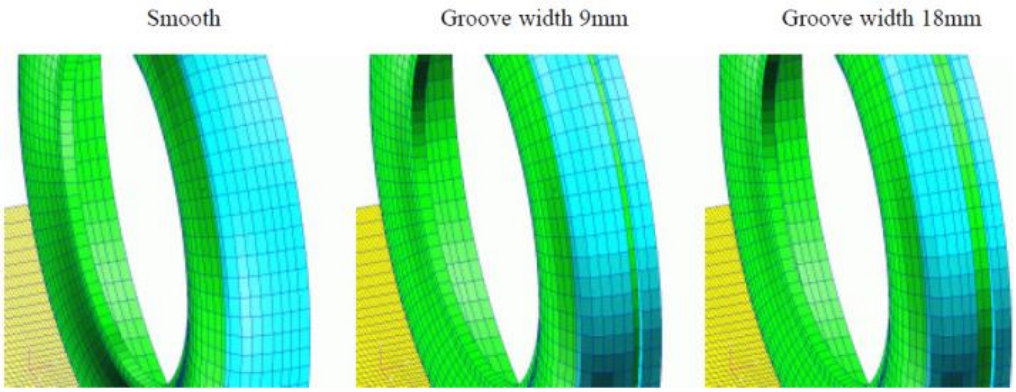

Figure A- 1: Different Groove width in longitudinal pattern [7]

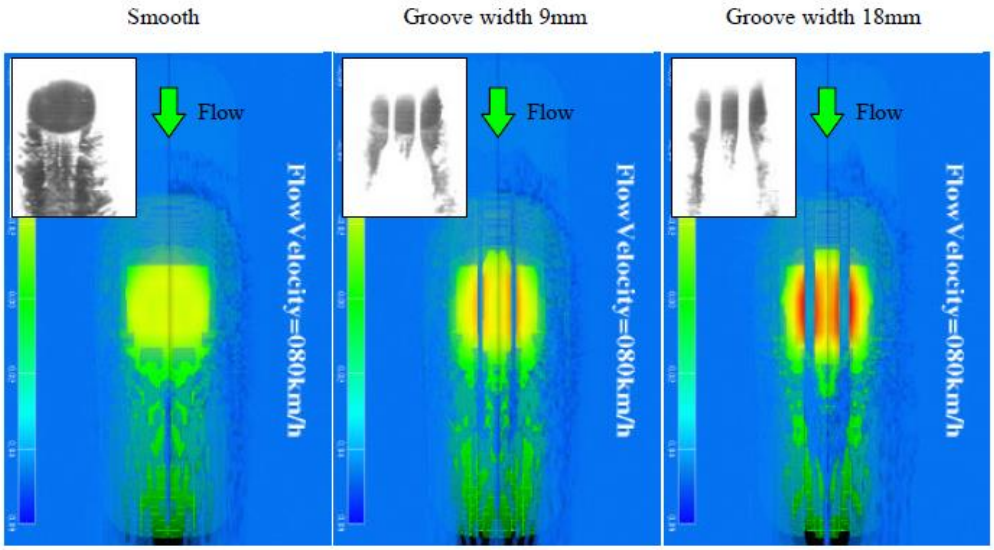

Figure A- 2: Flow profile through different Groove width [7]

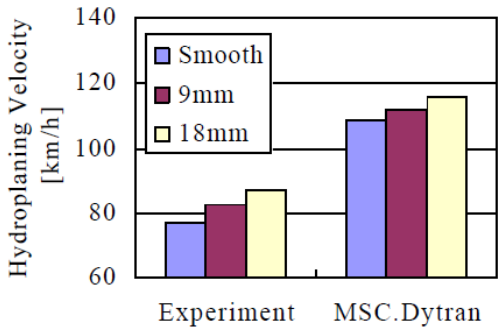

Figure A- 3: Comparison of the experimental data with modeling results [8]

Kumar *et al.* 2009 have studied the hydroplaning phenomena for a tire running on a wet surface. The tire experiences multiphase flow at the velocity U in respect to the tire, as shown in Figure A-4. They studied the effects of tire groove geometry on hydroplaning and showed that how hydroplaning varies with different groove width, depth and spacing. (Figures A-5-A-7)

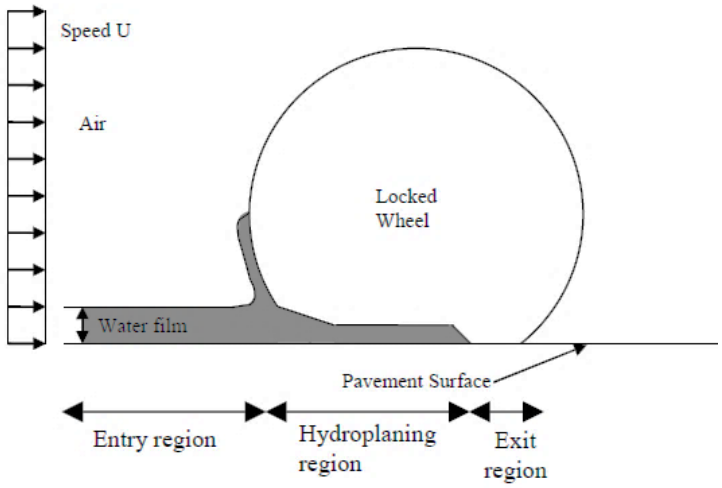

Figure A- 4: Schematic of tire-road model in moving tire's reference frame [2]

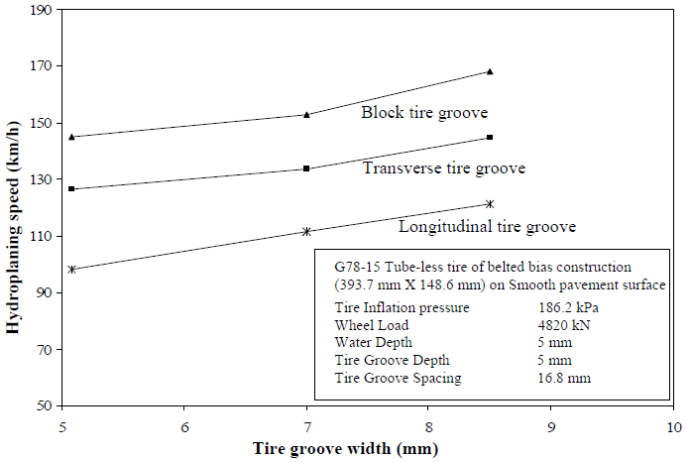

Figure A- 5: Effect of tire groove width on hydroplaning speed [2]

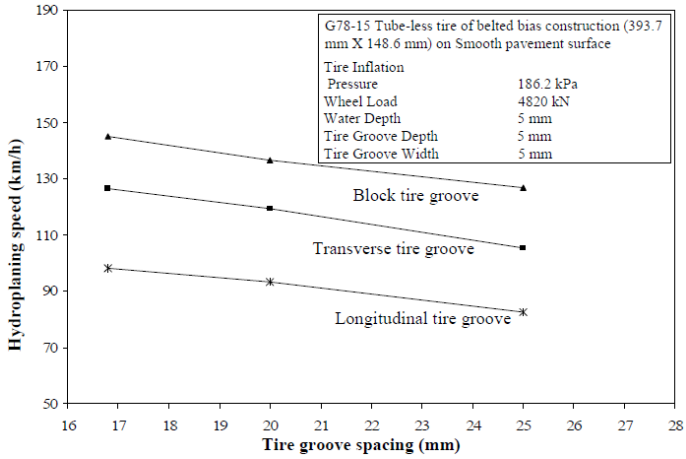

Figure A- 6: Effect of tire groove space on hydroplaning speed [2]

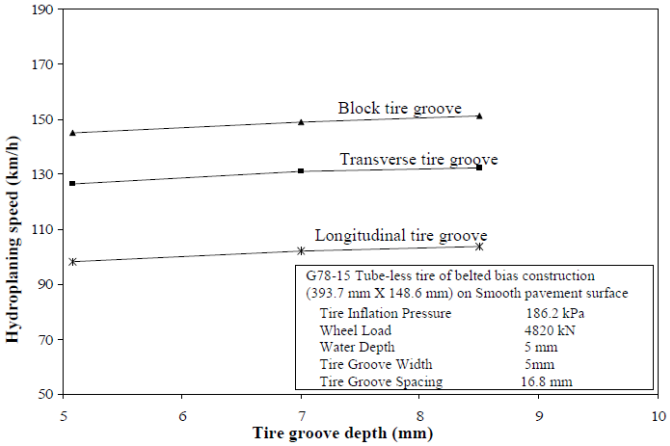

Figure A- 7: Effect of tire groove depth on hydroplaning speed [2]

As results are shown, it can be concluded that among the studied parameters, groove width is the most effective parameter, in terms of increasing hydroplaning speed.

Based on the tire-road studies, it can be concluded that:

- Tire grooves can drag the water through and increase the hydroplaning speed.
- Block and transverse patterns show better performance than longitudinal in terms of hydroplaning speed up to 53.7% and 29%, respectively.
- Groove width is the most effective parameter. Groove width had 23.7% increase over the groove width range studied.
- Groove spacing showed 20.1% and groove depth showed 5.8% increase over the groove width and depth range studied.
- Based on the tire-road analogy, wider groove (groove #2) is selected among other patterns for the galvanizing bath roll.

Another important lesson from tire-road analogy is that the strip should be in direct contact with the roll. It can be concluded that to keep the production rate of galvanized steel constant, the line tensioning force has to be more than the hydrodynamic uplift force. The following section will study the strip-roll separation using a force analysis.

References

[1] Ong, G.P., Fwa, T.F. & Asce, M., 2006, Transverse Pavement Grooving against Hydroplaning . I : Simulation Model. , (June), pp.441–449.

[2] Kumar, S. (2009), Analyzing Effect of Tire Groove Patterns on Hydroplaning Speed, Journal of the Eastern Asia Society for Transportation Studies.

[3] Horne, W.B and R.C Dreher. 1963, Phenomena of Pneumatic Tire Hydroplaning, NASA TN D-2056.

[4] Gallaway, B. M., Ivey, D. L., Hayes, g. G., Ledbetter, W. G., Olson, R. M., Woods, D. L. and Schiller, R. E. 1979, Pavement and Geometric Design Criteria for Minimizing Hydroplaning. Federal Highway Administration Report, No. FHWA-RD-79-31, Texas Transportation Institute, Texas A&M University, USA.

[5] Maycock, G. 1967, Experiments on Tyre Tread Patterns, Road Research Laboratory Report LR 122.

[6] Gengenbach, W. 1968, Experimental Investigation of Tires on a wet Roadway ATZ, Vol. 70, No.9.

[7] Okano, T. & Koishi, M., Hydroplaning Simulation using MSC . Dytran.

Curriculum Vitae

Name:	Amir Kargar Neghab
Post-secondary Education and Degrees:	The University of Western Ontario London, Ontario, Canada 2012-2015 M.E.Sc.
	Tarbiat Modares University of Tehran Tehran, Iran 2004-2004 M.E.Sc.
	Iran University of Science and Technology Tehran, Iran 1999-2004 B.E.Sc.
Honours and Awards:	Western Graduate Research Scholarship 2012-2015
Related Work Experience	Teaching Assistant The University of Western Ontario 2012-2015